Electrical Machine Initial Design and Computational Tool

Master's thesis in Automotive Engineering

AKASH CHANDRAKANT ULVEKAR

KOUSHIK DAMODARA SHENOY

DEPARTMENT OF AUTOMOTIVE ENGINEERING

CHALMERS UNIVERSITY OF TECHNOLOGY
Gothenburg, Sweden 2025
www.chalmers.se

Master's thesis 2025

Electrical Machine Initial Design and Computational Tool

AKASH CHANDRAKNT ULVEKAR
KOUSHIK DAMODARA SHENOY

CHALMERS
UNIVERSITY OF TECHNOLOGY

Department of Mechanics and Maritime

Chalmers University of Technology
Gothenburg, Sweden 2025

Electrical Machine Initial Design and Computational Tool
AKASH CHANDRAKNT ULVEKAR
KOUSHIK DAMODARA SHENOY

Supervisor (AVL): Przemyslaw Radecki
Examiner (Chalmers): David Sedarsky

Master's Thesis 2025
Department of Automotive Engineering
Chalmers University of Technology
SE-412 96 Gothenburg
Telephone +46 767096433, +46 761527767

Typeset in LaTeX
Printed by Chalmers Reproservice
Gothenburg, Sweden 2025

Electrical Machine Initial Design and Computational Tool
AKASH CHANDRAKANT ULVEKAR
KOUSHIK DAMODARA SHENOY
Department of Automotive Engineering
Chalmers University of Technology
AVL

Abstract

Electric and hybrid electric vehicles widely use Interior Permanent Magnet Synchronous Machines (IPMSM) due to their high torque and power densities. The initial design phase of these electrical machines are critical as they affect the performance, efficiency and cost-effectiveness. This thesis explores the development and application of a Python-based computational tool for the initial design of IPMSMs, aiming to achieve optimal machine performance while reducing dependency on iterative Finite Element Method (FEM) solutions. The scope of the research was to develop a robust framework that bridges theoretical design principles with practical computational methods, aiding innovation in electrical machine engineering.

An analytical approach was adopted for the preliminary design, focusing on the relationship between machine sizing and performance parameters. Preliminary designs were derived using geometrical constraints and mathematical equations. These designs were validated through Magnetic Equivalent Circuit (MEC) models and sensitivity analysis, with results further corroborated by FEM simulations.

The study is centered on two case studies: a MotorCAD template and a journal model. The Python tool demonstrated high accuracy, with sizing parameters closely matching those from MotorCAD and the journal model. Sensitivity analysis was conducted to evaluate the impact of variations in air-gap thickness, magnet width, pole-arc to pole-pitch ratio, and magnet strength on machine performance. The results showcased consistent trends between the Python tool and MotorCAD, emphasizing the tool's reliability and robustness.

The computational tool made it computationally efficient by enabling rapid prototyping and reduced iteration time. This work highlights how the tool can efficiently and accurately design IPMSM, providing a solid foundation for future advancements in electrical machine engineering.

Keywords: analytical approach, finite element method, IPMSM, machine sizing, magnetic equivalent circuit, MotorCAD, python-based computational tool

Acknowledgments

We would like to extend our gratitude to our examiner, Associate Professor at Chalmers University of Technology Dr. David Sedarsky, for his constant support, feedback, and guidance throughout the project, which improved the quality of the work.

We are grateful to our supervisor, lead engineer at AVL Mr. Przemyslaw Radecki, for his mentorship, continued support, encouragement, and expert insights that helped us steer the project in the right direction.

We also wish to thank Mr. Jan Nyberg, AVL Manager, for providing us with this opportunity, necessary resources, and a conducive environment for this research.

A special thanks to Mr. Punit Acharya, Software Development Engineer at AVL, for his technical expertise and valuable suggestions that significantly contributed to the depth and rigor of this work.

Finally, we would like to thank our family and friends for their unwavering support and encouragement throughout this journey.

Akash Chandrakant Ulvekar, Gothenburg, January 2025
Koushik Damodara Shenoy, Gothenburg, January 2025

List of Acronyms

The following is a list of abbreviations that have been used in this thesis, arranged alphabetically:

AC	:	Alternating Current
BEMF	:	Back Electromotive Force
BEV	:	Battery Electric Vehicle
DC	:	Direct Current
EM	:	Electrical Machine
ID	:	Irreversible Demagnetization
IM	:	Induction Machine
IPMSM	:	Interior Permanent Magnet Synchronous Machines
LCM	:	Least Common Multiple
MEC	:	Magnetic Equivalent Circuit
OP	:	Operating Point
PM	:	Permanent Magnet
PMSM	:	Permanent Magnet Synchronous Machines
RM	:	Reluctance Machines
SPMM	:	Surface-mounted Permanent Magnet Synchronous Machines

Contents

List of Figures

List of Tables

1
Introduction

Environmental concerns due to climate change driven by global warming have received significant attention. Efforts to reduce the carbon footprint and advance towards climate-neutral vehicles have led to rapid advancements in electric propulsion systems. The global transportation landscape is significantly transforming, with e-mobility at its forefront [1]. The surge in electric vehicles (EVs) on roads worldwide marks a pivotal shift towards sustainable transportation. Governments and industries invest heavily in e-mobility solutions to combat climate change, reduce carbon emissions, and promote energy efficiency. This boom is driven by technological advancements, increasing environmental awareness, and regulatory pressures to reduce dependence on fossil fuels.

At the heart of this e-mobility revolution lies the Electrical Machine (EM), a critical component that directly impacts electric vehicles' performance, efficiency, and reliability [1], [2]. The efficiency of the electric motor determines the vehicle's range, acceleration, and overall energy consumption [1], [2]. Optimizing motor performance is essential for developing competitive and sustainable EVs [1], [2]. Research and development in motor technologies are crucial to meet the demands of modern e-mobility.

1.1 Background

EMs convert electric energy produced by the battery into mechanical energy required by the wheels [3]. Hence, these machines must be designed to satisfy the basic characteristics that facilitate the vehicle traction requirements [1], [2]. The rapid evolution of the e-mobility market demands continuous innovation in EM design to develop efficient, powerful machines that are also compact and cost-effective [1], [2]. These requirements include high torque density and power density, high torque at low speeds, wide speed range, high efficiency over wide speed range and torque range, affordable cost, and robustness for the machine's application [1], [2].

There are several machines available in the market (i.e., induction machines, Permanent Magnet Synchronous Machines (PMSM), Reluctance Machines (RM), etc.) that satisfy the vehicle requirements [1], [2]. However, the Interior Permanent Magnet Synchronous Machine (IPMSM) using Alternating Current (AC) is the most popular machine for its several advantages and production ease [1]. It is a type of PMSM with a magnet embedded within the rotor and stands out for its high efficiency, power and torque densities, and precise control [2].

EM designs are mainly facilitated by advanced numeric Finite Element Method (FEM) software like Motor-CAD and ANSYS Maxwell [4]. However, using such tools effectively for design requires well-defined initial design parameters as input to optimize the machine sizing [5] and performance requirements.

The challenge lies in balancing the machine performance while addressing issues such as thermal management, durability, and material costs [6]. This research is critical to advancing the capabilities of electric vehicles, making them more accessible and appealing to a broader audience.

The goal of this proposal is to improve the machine design process with reliable numeric calculations using analytical design equations and obtain the reference values for validation in FEM.

1.2 Aim

To develop a computational environment for Interior Permanent Magnet Synchronous Motors (IPMSM) by establishing the analytical relationships between machine sizing parameters and performance parameters using the Python platform.

1.3 Project Concept

1.3.1 Objectives

The following approaches were followed to achieve the goal set by the thesis.

1 To establish analytical relations between machine performance parameters (torque, speed, and power) and machine sizing parameters (dimensions of the stator, rotor, and their components) and electromagnetic analysis.

2 To generate an algorithm with machine performance parameters as input data and derive the machine sizing parameters as output using Python.

3 To validate the derived machine sizing parameters using the FEM tool.

4 To provide a design guidebook with a systematic design procedure for electrical machines.

1.3.2 Hypothesis

1 Utilizing the computational tool in the machine design process significantly reduces the time required for evaluating multiple design scenarios, enabling quicker decision-making compared to traditional computational methods.

2 Engineers who use the computational tool can more readily adjust design parameters and test various configurations of an IPMSM, leading to greater flexibility and precision in achieving design objectives.

3 The computational tool can be effectively adapted to different machine applications, enhancing its versatility and applicability within diverse engineering contexts.

2

Theory

The global need to reduce carbon footprint has revolutionized the automotive industry. The focus on developing climate-neutral vehicles has received increased attention partly due to the need for an alternative fuel source. Climate-neutral vehicles may be defined as those that do not release greenhouse gases.

Electrical Machines (EM) and drives are among the leading enabling technologies for climate-neutral vehicles [1]. They became popular among scientists and researchers in the 19th century [3]. However, their development has been rapid recently as there is a need for high-performance machines.

2.1 Climate Neutral Vehicles and Propulsion System

There are three leading technologies for climate-neutral vehicles: fully electric, hybrid, and fuel cell [1]. These vehicles use different systems to generate electrical energy and use EM for propulsion.

A climate-neutral vehicle must overcome many forces, including the friction between the wheel and the road surface, the aerodynamic drag force, and the force due to its weight and acceleration. The EM provides the required energy to overcome these forces through torque and power [1]. Torque is the ability of the vehicle to begin motion, and power is the ability of the vehicle to accelerate quickly.

There are basic characteristics that need to be satisfied by the EM for traction applications [1], [2]. Figure 2.1 illustrates the ideal torque-power-speed curve of an EM where along the x-axis is the speed (in revolutions per minute (RPM)) and along the y-axis is the torque (in Nm) highlighted in blue. The power (in W) is highlighted in red. The figure shows that torque is high at low speeds, constant till base speed, and decreases at high speeds. Power rises with speed, peaks at base speed, and stabilizes or drops thereafter.

When designing a machine, peak torque and power are considered to ensure that the machine can handle extreme operating conditions, i.e., high power and torque operations to give reliable output without wear and tear. Machines designed with peak performance requirements are durable, reliable, robust, and meet the performance demands during extreme conditions.

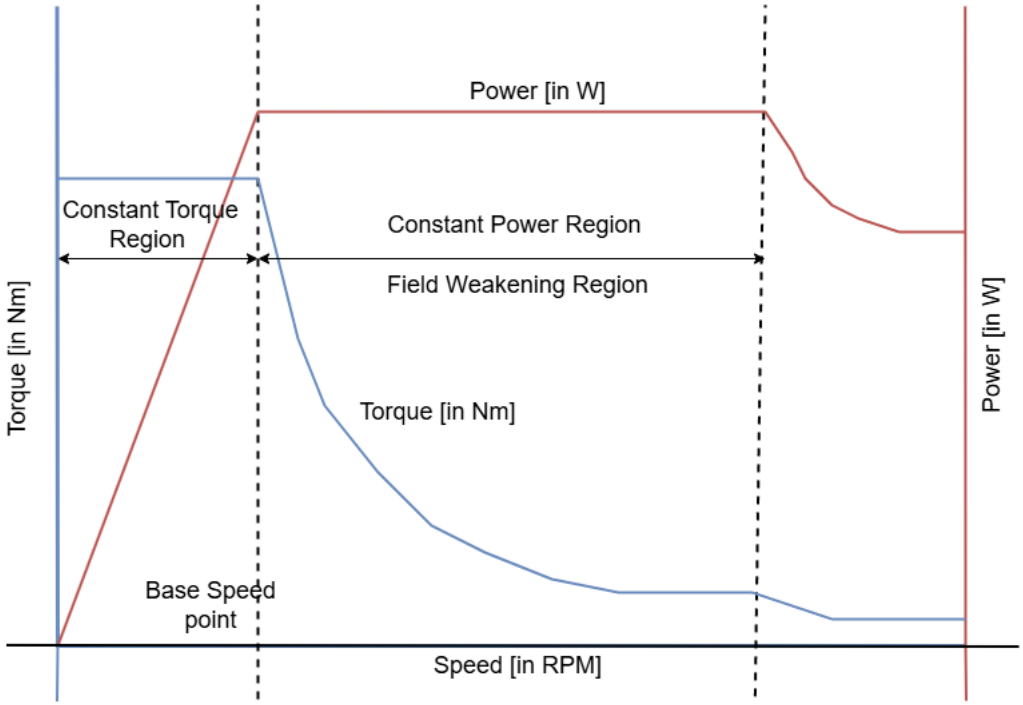

Figure 2.1: Illustration of Torque-Power-Speed Characteristics

The EM is an important component in the driveline that provides the necessary propellant forces for the vehicle and is responsible for its motoring action [2]. It utilizes the electrical energy provided by the battery systems and converts it to mechanical energy in the form of torque, power, and speed [2], [3].

Energy conversion in these machines happens via magnetic energy by applying electromagnetic principles [3]. The fundamental concept focuses on electromagnetic induction, where a current-carrying conductor in a magnetic field experiences a force [2], thereby generating the mechanical energy required for the load [7].

2.1.1 Classification of Electrical Machines

The EMs are classified according to the power used, namely, Direct Current (DC) and Alternating Current (AC) [3]. The most popular machines used for traction applications are DC machines. In contrast, Induction Machines (IM), Permanent Magnet Synchronous Machines (PMSM), and Switched Reluctance Machines (SRM) use AC as a power source [1], [2].

In electric propulsion systems, DC drives were prominent due to their torque-speed characteristics and simplicity of control. However, their bulky construction, low efficiency and reliability, and higher maintenance costs made them a less viable option [2]. Furthermore, advancements in machine technology, particularly the development of rugged solid-state power semiconductors, facilitated the emergence of AC machines in the automotive industry [2], phasing out DC drives.

The authors in [2] also investigated the potential of SRM in the propulsion system of HEV. Although these machines have simple control techniques and good torque-speed

characteristics, they are outweighed by their disadvantages. These machines generate excessive bus current ripple, electromagnetic interference (EMI), acoustic noise, and torque ripple that are critical for vehicle operation making them unsuitable for the presented application.

IM and PMSM are the most popular EMs using AC machine technology in propulsion systems [2]. A general vehicle requirement is for the machine's constant power region to extend 4 to 5 times the base speed. The breakdown torque limits this extended region in an IM. Further, the IMs do not perform efficiently at high-speed operation, due to rotor winding and copper losses [2]. On the other hand, the PMSM can outperform these drawbacks, making them competitive in the market. The PM machines, based on the location of the magnets [1], are classified into Surface-mounted Permanent Magnet Machines (SPMM) and Interior Permanent Magnet Synchronous Machines (IPMSM).

In SPMM, the Permanent Magnets (PMs) are present on the surface of the rotor in the air gap [8]. This produces higher magnet torque but at the cost of power capabilities in the field weakening region. This is because of low inductance and the absence of reluctance torque. In comparison, the IPMSM has higher power capabilities due to high inductance at the field weakening region, extending the power-speed characteristics. The presence of reluctance torque due to saliency optimizes the volume of the magnet used to obtain the same torque output. The added advantage of high efficiency and ease of production [3] makes IPMSM a more popular choice for electric propulsion systems.

2.2 Interior Permanent Magnet Synchronous Machines

The IPMSM is a topology of a PMSM where the magnet is embedded within the rotor core [1]. In an IPMSM, the rotor is the rotating component placed within the stator, and the magnets are placed in a position to efficiently utilize the magnet grade factor [3]. The stator contains slots with windings [3] acting as primary coils.

The AC passing through the primary coils produces a magnetic field that interacts with the field generated by the magnet [2]. When the AC is supplied to the stator windings, it creates a rotating magnetic field [2]. The rotor, which contains PMs, aligns itself with this rotating magnetic field due to the magnetic attraction and repulsion forces. As the rotor rotates, it generates torque, which drives the mechanical load connected to the machine shaft [2] and thus causes the motoring action.

Figure 2.2 describes the front and side view of the IPMSM [9]. The rotor core provides mechanical support for the PMs and is usually made of laminated magnetic material to reduce eddy current losses [9]. The rotor core may also have slots for inserting the PMs. The stack length is the length of the machine in the axial direction [9], which defines the volume of the rotor.

The thickness of the air gap is the hollow distance between the stator's core and the rotor's core [9].

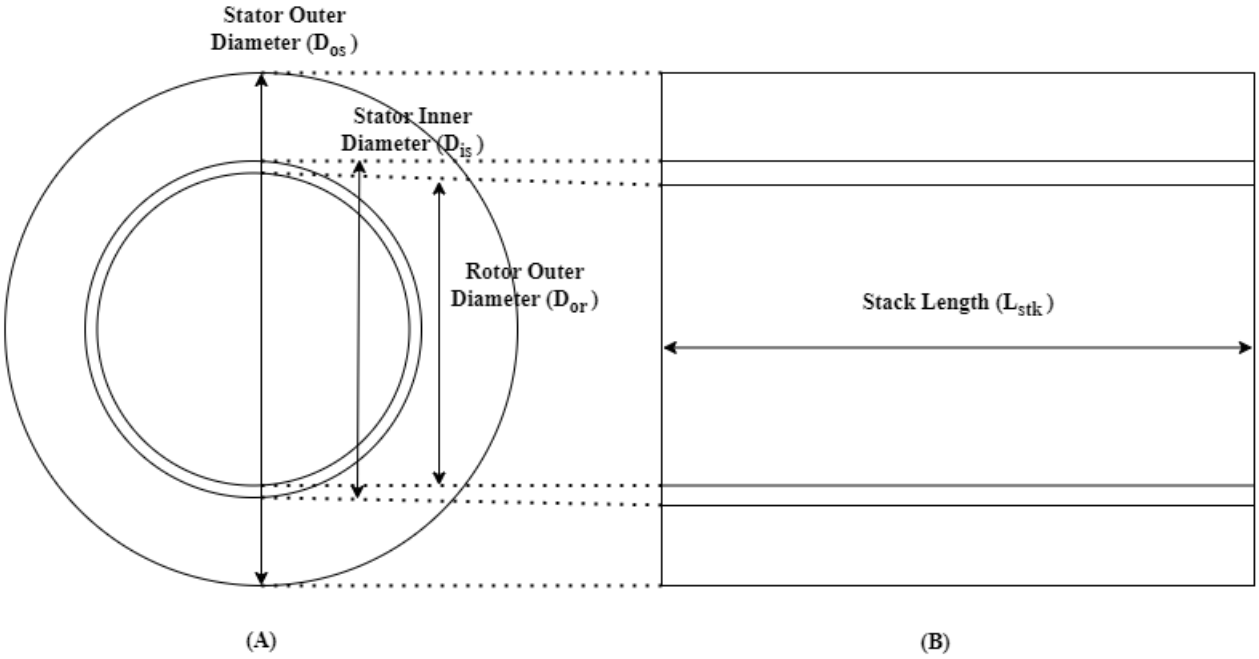

Figure 2.2: (A) Front View (B) Side View of Interior Permanent Magnet Synchronous Machine

The stator is an essential part of EM, serving as the stationary component that creates the rotating magnetic field that interacts with the rotor. The stator comprises various components such as the stator core, tooth, and slot, and houses the winding, as seen in Figure 2.3 [10].

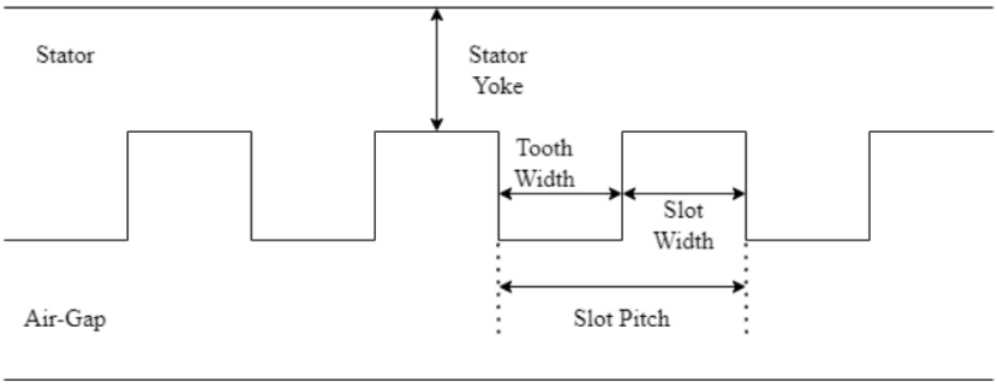

Figure 2.3: Stator and its Components

The stator core serves as the magnetic circuit path for the magnetic field. The stator's outer diameter defines the boundary of the core. The core must be mechanically robust to withstand the forces generated during the operation [11]. It is typically made from laminated electrical steel or iron due to its high magnetic permeability and its ability to reduce eddy current and hysteresis losses [12]. As the stator contains windings, they must also have a proper cooling system to dissipate heat generated due to losses [12].

The tooth is an essential part of the stator that protrudes outwards directing and concentrating the magnetic flux into the air gap between the stator and the rotor [13]. Since the flux lines pass through the tooth, it affects the machine's magnetic saturation, flux distribution, and electromagnetic performance. The slots are the grooves in the core between the teeth designed to accommodate the windings and ensure proper electromagnetic interaction with the rotor [13]. The number of slots in the core determines the spatial distribution of the windings. It affects the machine's electromagnetic characteristics, such as torque ripple, cogging torque, and winding inductance [12]. More slots can improve the machine's performance but can increase the complexity and the cost [14].

The windings in the core refer to the conductive wires wound in specific patterns on the stator core of an EM. They can be categorized based on various aspects, such as the machine type, winding arrangement, and the nature of the current. The commonly used winding types are concentrated and distributed.

Concentrated windings have a conductor wound over one tooth, i.e., one tooth carries exactly one winding. These windings are easy to construct, provided the stator dimensions are known. They produce high torque and create a high magnetic field; however, they have lower efficiency, which limits their application to small servo motors [15]. Distributed windings have at least two teeth of the stator wound together, i.e., the winding is spread across multiple stator slots. The number of teeth wound by a single winding is called coil pitch. This winding configuration creates a more uniform magnetic field, reducing losses and vibrations [15]. Distributed windings have high synchronism, reducing torque ripple and noise [15].

In an IPMSM, the rotor contains PMs that are typically made of materials like neodymium-iron-boron (NdFeB) or samarium-cobalt (SmCo) [16], [17]. The design of rotor components focuses on the magnet volume and position to achieve high efficiency.

Figure 2.4 illustrates the different parts of the rotor that need to be evaluated by the analytical expressions established.

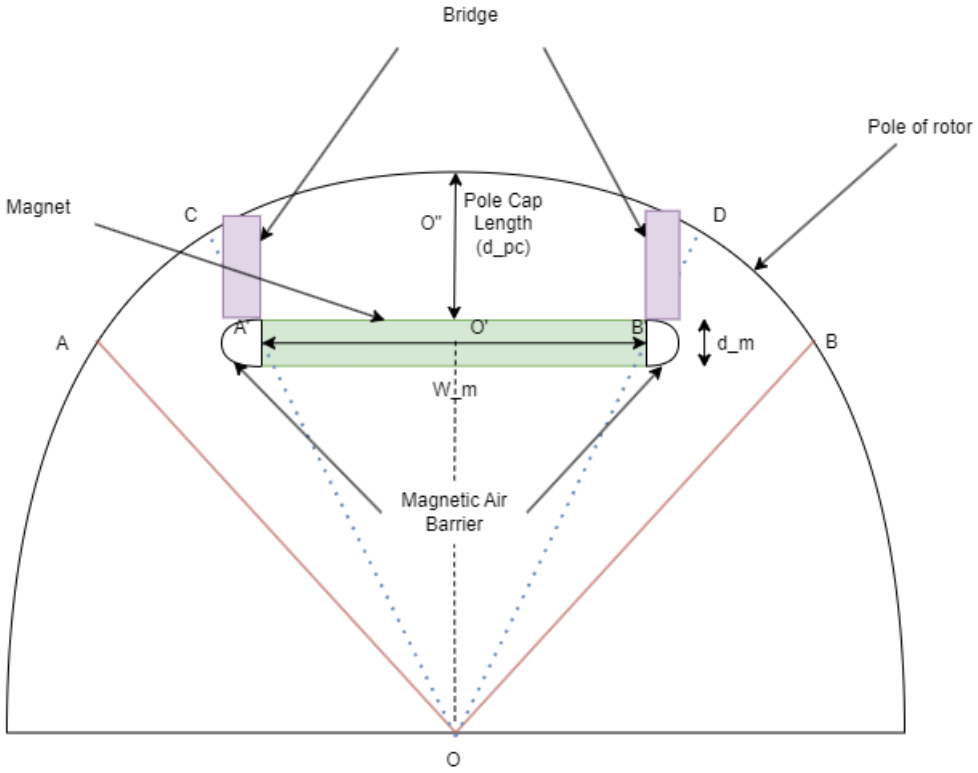

Figure 2.4: Front View of the Rotor and its Components

The pole defines the number of PM pole pairs present in the rotor that can be in the sequence of 2, 4, 6, and so on. This is because a magnet has two poles (North and South poles) [18]. Pole pitch is the arc length of the rotor core that subtends a pole (in Figure 2.4 arc AB), and pole arc is the arc length of the rotor core that subtends the magnet (in Figure 2.4 arc CD) [12], [19], [20]. The ratio of pole arc to pole pitch limits the space in the rotor core for the magnet's placement, influencing the magnet's volume and position.

The pole cap is the point on the circumference of the rotor perpendicularly above the magnet. The distance from the pole cap to the magnet is the thickness of the pole cap (in Figure 2.4 d_{pc}) also called pole-cap length. This acts as the passage for the magnetic field produced to flow across the air gap [21], [22]. The rotor core contains a space at each end of the magnet called the magnetic air barrier. The bridge is the thickness of the rotor lamination between the magnetic air barrier and the circumference of the rotor. The bridge has two functions: preventing flux leakage that leads to cross-magnetization within the rotor core and reducing the inertial effect due to stress concentration. The rotor's material at the bridge is saturated, preventing the magnetic field from flowing through it, and thus reducing leakage [23].

2.3 Design of Electrical Machines

Designing an EM involves several methodologies, each with its advantages and limitations. The primary goal is to determine the optimal machine size and the specifications that meet the desired performance criteria. Some of the popular approaches include empirical,

numerical, and analytical techniques.

Empirical methods rely on experimental data and established design rules to design machines. These methods are often used by experienced engineers who draw upon past successes to inform new designs. While empirical methods can be effective, they may not always provide the most efficient or innovative solutions.

A numerical approach, such as Finite Element Analysis (FEA), is a generic modeling approach applied for design optimization and modeling of EMs [24]. This method offers the ability to model the magnetic field distribution in the rotor, stator, and air gap with high accuracy [4], which plays a significant role in understanding the performance characteristics of the machine. However, the major drawback of this method is the time-consuming calculations that render it unsuitable for the initial design phase.

Analytical methods involve mathematical models and equations to estimate machine parameters. These methods offer a more streamlined approach to machine design, allowing for quick calculations and adjustments [5]. By leveraging fundamental physics and engineering principles, analytical methods can provide accurate sizing parameters with minimal computational resources.

2.4 Torque in IPMSM

The torque generated in an IPMSM is attributed to two components: the magnet torque produced by the Magneto Motive Force (MMF) due to the magnetic field distribution generated by the PM and reluctance torque due to the saliency effect [3], [11]. Figure 2.5 [8] represents the torque components in IPMSM, and depicts the torque produced by a magnet in blue, the reluctance torque in red, and the resultant torque in black colours.

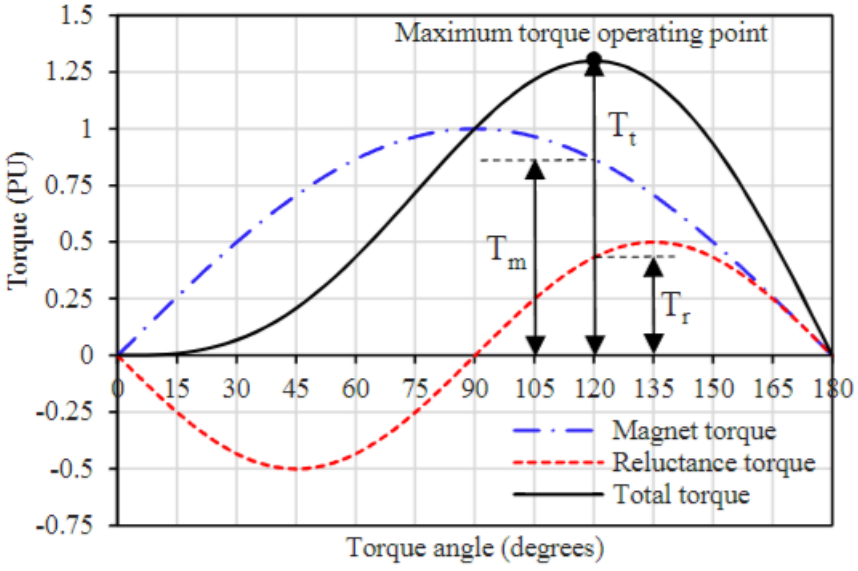

Figure 2.5: Components of Torque of IPMSM

Torque per Rotor Volume (TRV) is defined as the machine's capability to produce torque limited by its volume [25]–[27]. Table 2.1 [26] gives a range of reference values of TRV based on the application of the machine designed. The higher the value of TRV, the smaller the rotor volume. A value is chosen based on various constraints, such as the type of cooling method and the area of location where the machine is used [26], [28].

Table 2.1: TRV Range of Values for Different Machines

Type of Machine	**TRV** ($\frac{kNm}{m^3}$)
Small totally enclosed motors (ferrite)	7 - 14
Totally enclosed motors (rare Earth magnets)	14 - 42
Integral hp industrial motors	7 - 30
High-Performance servo motors	15 - 50
Aerospace machines	30 - 75
Large liquid-cooled machines	100 - 250

The aspect or shape ratio defines the ratio of the stack length to the rotor's pole pitch. This value is limited by the machine's torque, speed, and stability [25]. Based on the torque and speed requirements, machines with low aspect ratios tend to be more compact and produce higher torque at lower speeds. As they have larger diameters, the torque arm is high, delivering higher torque output.

Machines with higher aspect ratios are suited for high-speed operations, as they have lower mechanical drag, which allows them to work efficiently at higher operating speeds [25]. In applications with strict space constraints, like electric vehicles or household appliances, the aspect ratio is chosen based on available installation space, often balancing compactness and desired performance.

Split ratio defines the ratio of the rotor's outer diameter to the stator's outer diameter. Machines with higher split ratios have larger rotors, which cause high vibrations and moments of inertia. Machines with lower split ratios have larger housings that dampen the vibration better [25].

The split ratio also provides insight into the machine type. Machines with a split ratio lower than one have a rotor inside the stator and are called internal machines while those with a split ratio greater than one have a rotor outside the stator and are known as external machines.

2.5 Magnetic Field Concepts

The two components responsible for creating magnetic torque are: a) PMs embedded in the rotor and b) current-carrying conductors in the stator slots. The magnetic field constitutes two vector components, namely, magnetic flux density ($\vec{B}$), and magnetic field intensity ($\vec{H}$) [3], [29]. The BH curve also called the demagnetization curve, is a graphical representation that describes the relationship between the flux density produced by the PM and field intensity [11], [30]. This describes the performance characteristics of the PM

[11], where the flux density is plotted along the y-axis and the magnetic field intensity is plotted along the x-axis [31]. Figure 2.6 represents the second quadrant of the hysteresis curve of magnet grade N42 at a working temperature of 20 ° C [32].

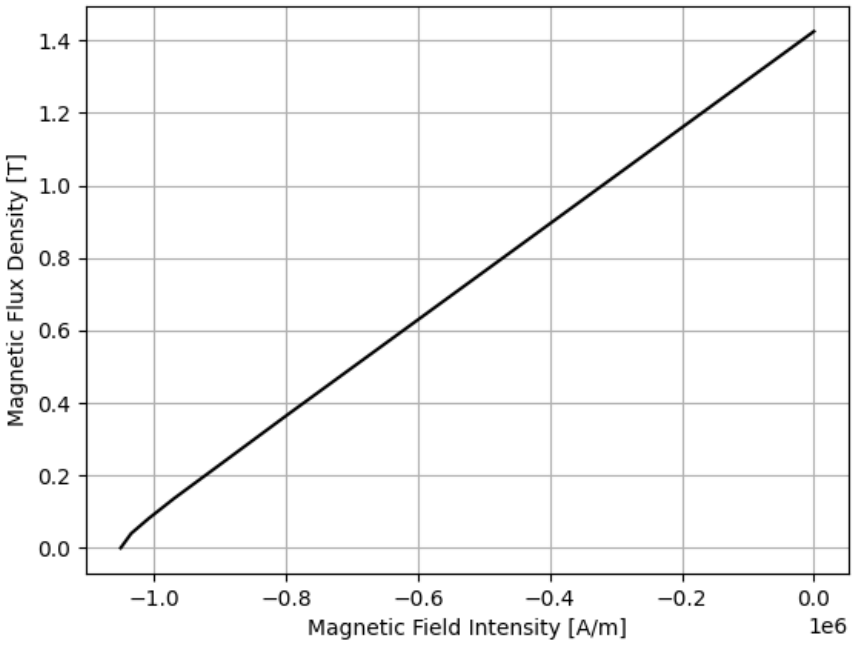

Figure 2.6: Image Describes the Second Quadrant of the Hysteresis Curve

The hysteresis curve is formed when a material is magnetized and demagnetized using an external excitation field [13]. When this field is shut off, the magnet relaxes or recoils, and the final point it attains is influenced by the permeance of the external surroundings. If the two ends of the magnetized material are shorted by an infinitely permeable material, the magnet's field intensity reaches zero ($\vec{H} = 0$). The flux density at this point is called remanence flux density ($\vec{B_r}$). $\vec{B_r}$ is the flux density of the magnet retained when the magnetizing field is removed and determines the strength of the magnetic material [16]. When the surrounding material of the magnet does not allow flux to flow out ($\vec{B} = 0$), the field intensity achieved across the magnet is called the coercivity [13]. This defines the strength of the magnetic material to remain fully magnetized when there is an opposing magnetic field.

$\vec{M}$ in Equation 2.1, is the residual magnetization factor [4]. Considering a linear demagnetization curve for a multi-pole machine in the second quadrant helps to deduce the $\vec{M} = \frac{\vec{B_r}}{\mu_0}$ [4], [33]. These parameters are mathematically represented by the following Equation 2.1.

$$\vec{B_m} = \mu_m * \mu_0 * \vec{H_m} + \mu_0 * \vec{M} \tag{2.1}$$

where μ_m and μ_0 [H/m] represent the permeability constants of magnet and vacuum respectively.

The magnetic flux is the density of flux lines distributed over a specific area, as described in Equation 2.2.

$$\phi_m = \vec{B_m} * A_m \tag{2.2}$$

where B_m represents the magnetic flux density [T], and A_m represents the area of the magnet across which the flux lines are distributed [m^2].

Magnetomotive force is generated due to a total change in the magnetic field intensity across the thickness of the magnet [3]. This is mathematically expressed as in Equation 2.3.

$$F_m = \vec{H_m} * d_m \tag{2.3}$$

where H_m is the magnetic field intensity [$\frac{A}{m}$], and d_m is the thickness of the magnet [m].

2.6 Permanent Magnet

The choice of magnets used in an EM is based on the cost and performance [13]. Material selection plays a significant role in the performance of the machines. There are many types of magnets, ranging from soft materials (ferrites) to hard materials (permanent magnets like rare-earth magnets) [11]. Soft materials are easy to magnetize and demagnetize and have a short hysteresis curve highlighted in green in Figure 2.7 [34]. Hence, these materials reach their saturation point earlier. On the other hand, hard materials have contrasting characteristics. They show a large hysteresis curve, as highlighted in red in Figure 2.7 [34], and attain saturation only when the magnet is highly stressed. This provides an advantage for high-performance machines where large currents are used at flux weakening point, which would prevent the risk of demagnetization of the PM [16], [35].

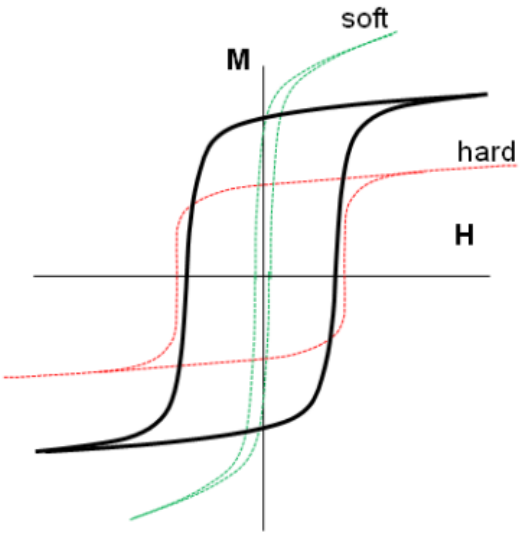

Figure 2.7: Comparison of Hysteresis Curve for Soft and Hard Materials

Hard magnets include PMs from rare-earth metals like Samarium cobalt and Neodymium [16]. Samarium cobalt magnets were initially used due to their high remanence, corrosion-resistive properties and high band range of operating temperature. However, the high cost of Cobalt made these magnets more expensive outweighing their advantages. Furthermore, neodymium magnets were introduced, which have linear properties and high remanence. They require less than three percent (< 3 %) or no cobalt, making them a cheaper alternative.

2.7 Permanent Magnet Modeling

The magnet's external and working conditions dictate its behavior. Modeling the operating conditions is critical for the design of PM [30]. Figure 2.8 describes the key terminologies to model PM. The black line represents the BH curve defined by the magnetic properties, the red line is called the load line, which is determined by the geometrical properties of the magnetic circuit, and the point of intersection of the two curves gives the operating point (OP) of the magnet at a specific working condition [32]. The encircled point on the BH curve is called the knee point.

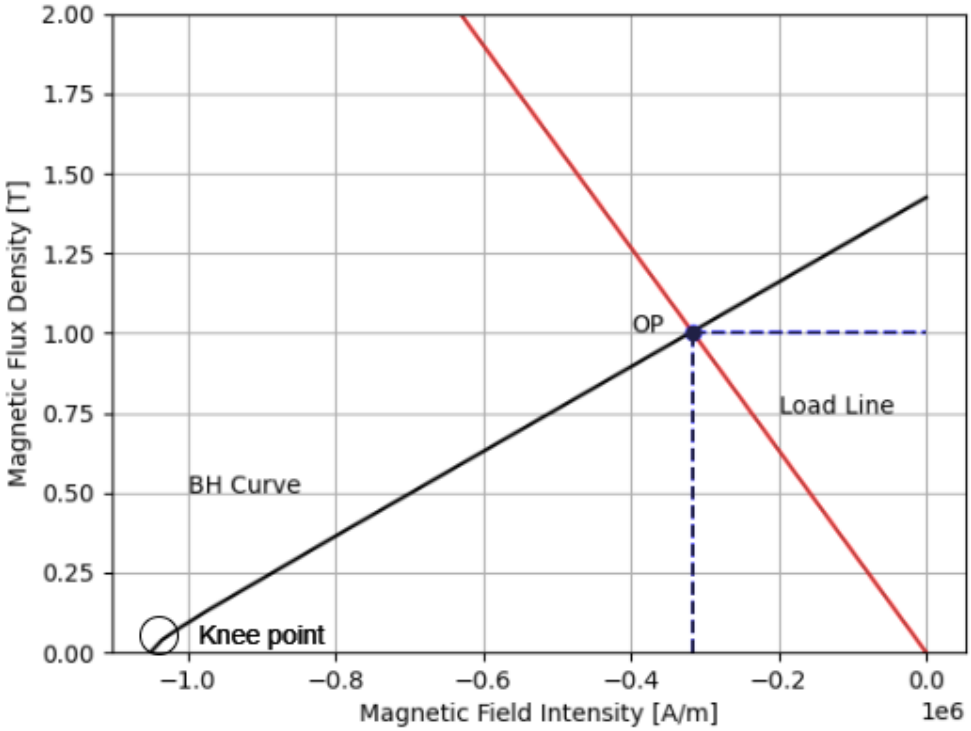

Figure 2.8: Description of Linear Modelling of PM

Irreversible Demagnetization (ID) is a phenomenon of a PM where it loses its initial remanence flux density due to operating conditions [30]. This occurs when PMs are highly stressed and the OP moves below the knee point. Higher temperature or external excitation impacts the OPs and the initial magnetic properties causing ID. Defining the BH curve based on operating conditions accurately helps to model PM and plays a role in

optimizing the design to prevent the risk of ID.

2.7.1 Temperature Effects

The magnet grade determines the initial magnetic properties and operational temperature range [32]. The BH curve depends on the working conditions. Persistent exposure of magnetic material to high temperatures degrades the material due to metallurgical changes within the magnet [31]. An increase in the temperature increases the kinetic energy of molecules in the magnet, and they tend to misalign faster. Hence, the magnet's hysteresis curve begins to shrink towards the origin as seen in Figure 2.9. This limits the energy available from the magnet as the knee point gets higher, increasing the chance of ID occurring [30], [35].

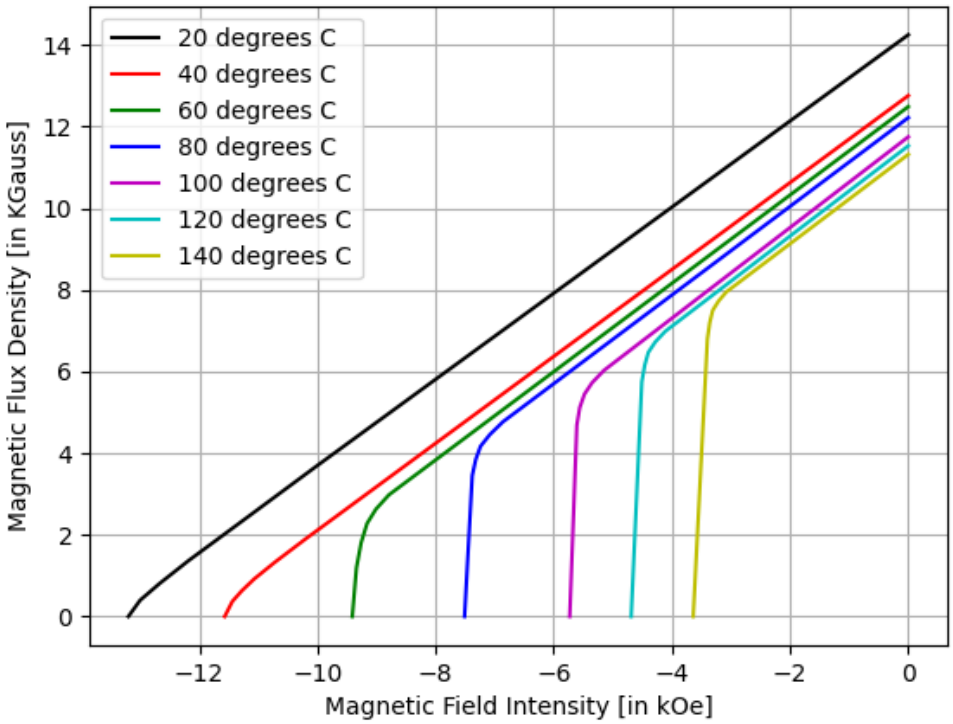

Figure 2.9: Illustration of the Temperature Effects on Demagnetization Curve

2.7.2 Effects of External Demagnetizing Field

The Demagnetizing Field (DF) in the IPMSM is caused by the current flowing through the stator coil. This acts as a delimiter to the flux density induction by the magnet in the air gap, impacting the magnet's OP. When DF is applied, the load line shifts to the left and closer to the knee point, increasing the risk of ID, as shown in Figure 2.10.

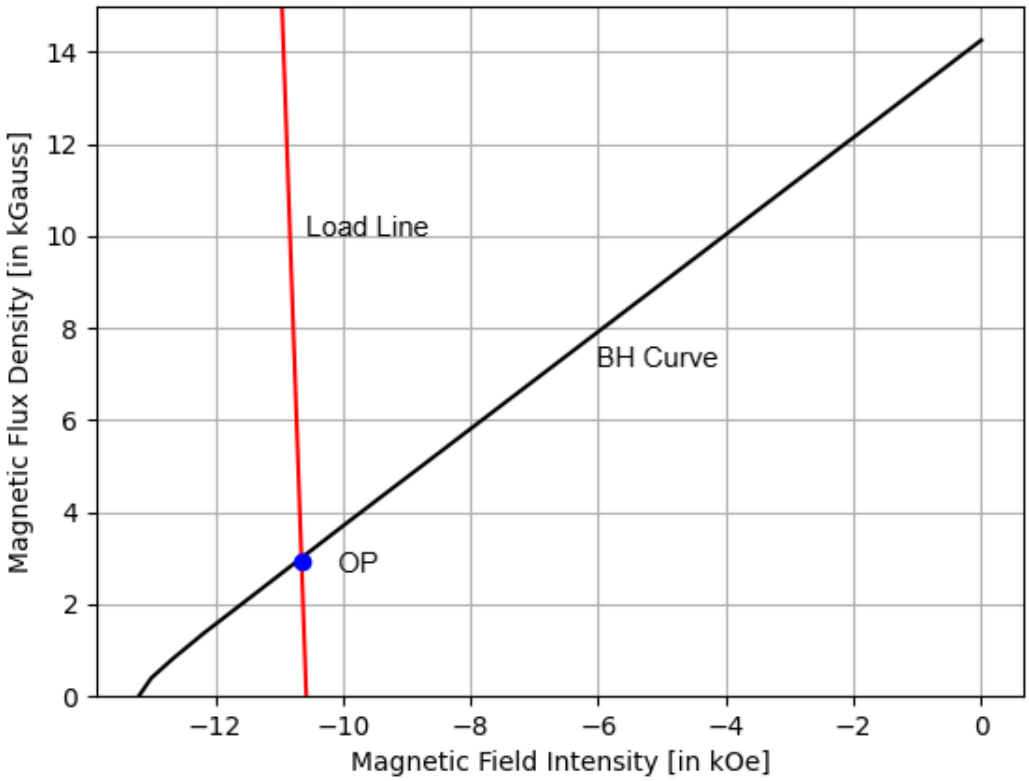

Figure 2.10: Illustration of Load Line with Excitation

When the DF $< H_{knee}$, the initial magnetic properties can be regained by removing the DF. This is because the magnet has not reached its limits, and therefore, the path of the recoil permeability remains through the BH curve [13], [30].

However, when the DF $> H_{knee}$, the magnet is said to have irreversibly demagnetized. Hence the magnet's new remanence flux density needs to be investigated by considering a new path of the recoil permeability [13], [30].

2.7.3 Investigation of Load Line

The machine's performance and efficiency depend on the effective usage of PMs, and accurately estimating its OP in the early design stage is beneficial. It provides critical information that helps to achieve and optimize the magnet volume for the required performance and prevent the risk of ID [30].

Investigating the load line involves assessing the impact of the magnet and air gap dimensions on its OP. The slope of the load line is given in terms of the permeance coefficient (P_c) [30]. The P_c dictates the magnet volume required for the desired output without the risk of ID [3] and signifies the ease with which the magnetic field lines flow from the magnet's north pole to its south pole through its external circuit.

2.7.4 PM Demagnetization Curve Modeling

There are two main approaches to modeling the demagnetization curve of the PM used in the IPMSM - a) linear model and b) exponential model [30], [36]. The complexity of the model increases, resulting in more dynamic and accurate results [37].

2.7.4.1 Linear Model

The linear modeling approach is the simplest mathematical model for characterizing the magnet's behavior. This modeling technique is divided into two parts - A) linear vertical slope and B) linear slope [30].

Demagnetization occurs when there is an increase in either the temperature or the DF. This usually occurs in the second quadrant of the hysteresis curve. The linear model is modeled using the fitting function as mentioned below -

$$B_d = \mu_0 * \mu_r * H_d + B_r \tag{2.4}$$

$$B_d = B_r + \mu_0 * H_t * (\mu_r - K_0) + \mu_0 * K_0 * H_d \tag{2.5}$$

B_d and H_d are the working points that signify the maximum energy the magnet can produce for the operating conditions [13]. Equation 2.4, called the linear slope model, represents the behavior of the magnet before it reaches the ID, that is, when $H_d \geq H_{knee}$, while Equation 2.5 represents the behavior of the magnet after ID has been reached where the $H_d \leq H_{knee}$. However, this model depicts the knee point as a sharp edge between the two curves, which could lead to errors [30].

2.7.4.2 Exponential Model

The exponential model eliminates the squareness in the previous approach, smoothens the knee point, and models the magnet behavior more accurately than the linear model [30]. However, this increases the complexity of the modeling approach and computational effort.

The fitting function requires additional coefficients K_1 and K_2 which define the sharpness of the knee point and fitting constant, respectively [16], [30]. It is characterized by Equation 2.6 [30].

$$B_d = B_r + \mu_0 * \mu_r * H_d - E * e^{K_1 * (K_2 + H_d)} \tag{2.6}$$

E is a constant term that helps in the unit conversion of magnetic properties and K_2 can be calculated using Equation 2.7 [30].

$$K_2 = \frac{\ln\left((B_r + (\mu_r - 1) * \mu_0 * H_c) * \frac{1}{E}\right)}{K_1} - H_c \tag{2.7}$$

The input to Equation 2.6 and Equation 2.7 are the magnetic properties defined by the chosen magnet grade and K_1.

2.8 Electromagnetic Calculations

Electromagnetic calculations involve studying the interaction between electric fields, magnetic fields, and forces in the machine. The flux density distribution must be studied in the air gap and at critical parts such as the rotor bridge, the stator tooth, and the stator yoke to evaluate the machine's design [13].

Several approaches exist to investigate the flux distribution within the air gap and understanding the electromagnetics of the electrical machine [38]–[42]. The analytical modeling approaches are solving Maxwell's equations, d-q axis modeling, and Magnetic Equivalent Circuit (MEC).

The first approach focuses on solving Maxwell's equation at different parts of the machine [42]. However, it does not account for iron saturation, which can significantly influence the magnetic field distribution and the losses in the EM. Additionally, the fringing effect and leakage are inaccurately modeled.

The d-q axis model applies coordinate transformation to simplify the electromagnetic equations that solve for flux linkage, inductance, and torque of three-phase motors [5]. However, this approach is less accurate when modeling saturation and non-linearities.

MEC is a prominent method implemented due to its simplicity and ability to capture the saturation of the magnetic field [13], [30]. This approach numerically solves magnetic field distribution at different parts of the EM using circuit network theory [42]. The complexity of the model can vary based on the number of elements considered in the circuit.

2.9 Magnetic Circuit Analysis

The machine's performance is influenced by the flux flow from the magnet in the rotor to the air gap [23]. This is measured in terms of permeance and reluctance properties [43], [44]. Figure 2.11 shows a simple example comparing EM with a C-core having a magnet, air gap, and coil carrying current [7], [42].

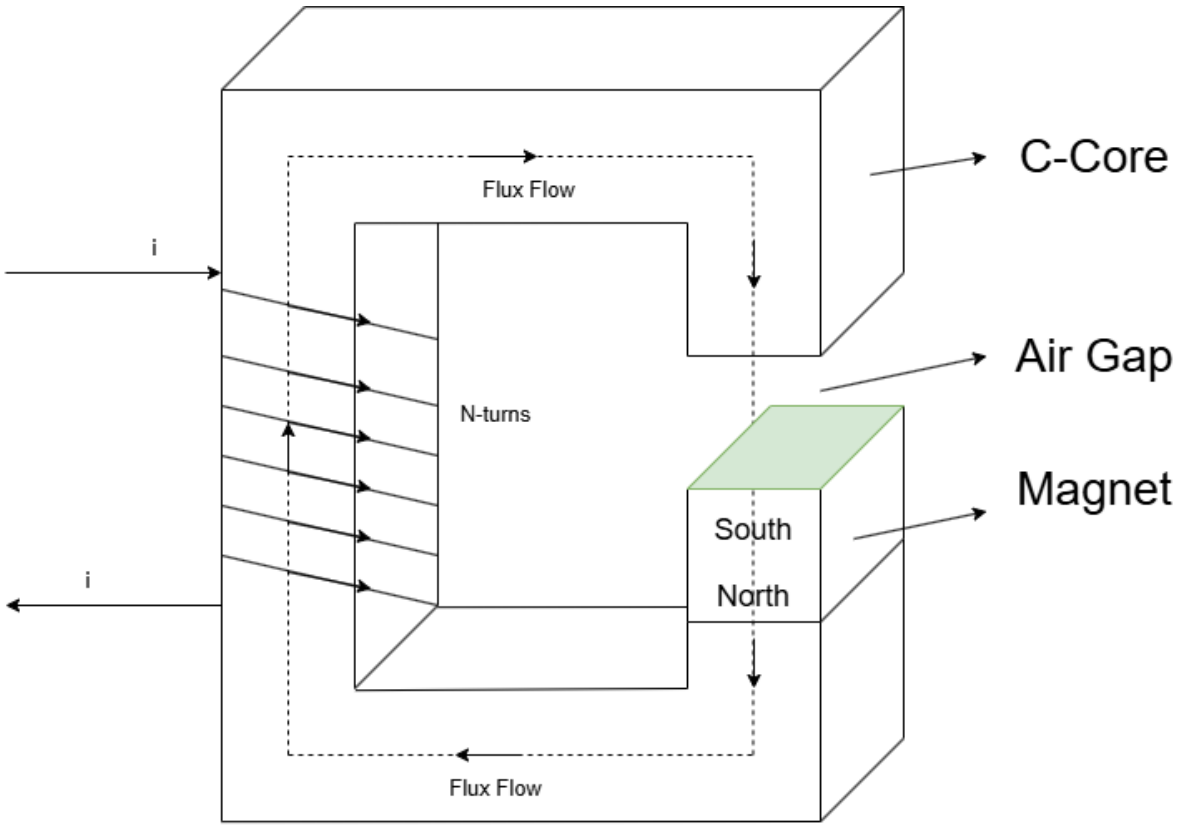

(a) Magnetic Field Circuit C-Core

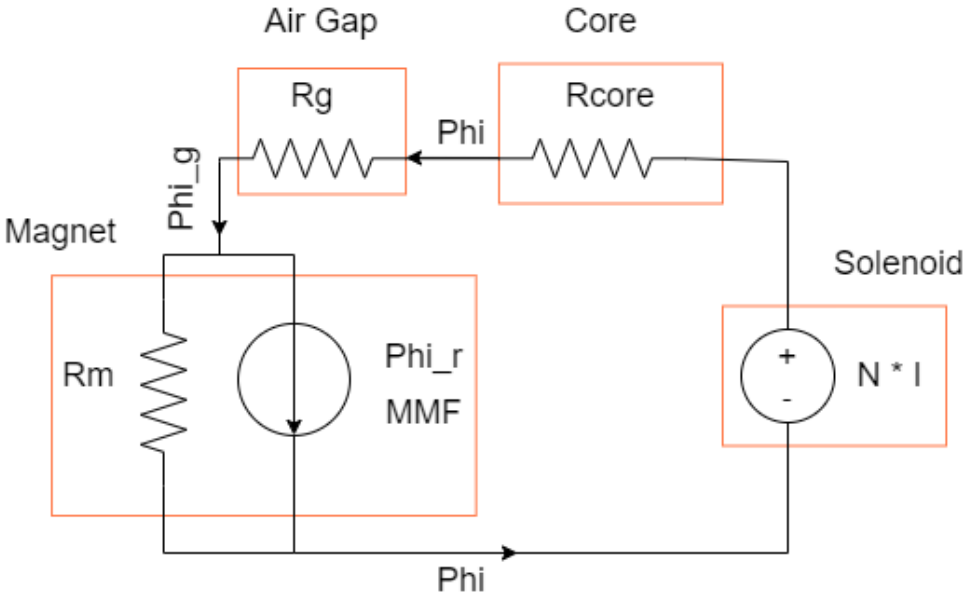

(b) Equivalent Magnetic Field Circuit

Figure 2.11: Illustration of Equivalent Magnetic Circuit of the C-Core

Figure 2.11a describes the C-core setup, while Figure 2.11b, describes its equivalent circuit. The C-Core is made of magnetic material (iron-core or stainless steel) with a copper coil wound around it. The magnet is placed on the core with the south pole facing the air gap and the north pole towards the core, creating a closed path for the magnetic field.

Considering the analogy mentioned in Table 2.2 [45]–[47], an equivalent circuit is deduced and modeled based on the MEC theory [7], [42].

Electric Circuit	**Magnetic Circuit**
ElectroMotive Force (EMF)	MagnetoMotive Force (MMF)
Resistance (R)	Reluctance (R)
Current (I)	Flux (ϕ)

Table 2.2: Analogy Between Electrical and Magnetic Terms

Permeance is measured by the ease of flux flow through different materials in a magnetic circuit and this can be represented as the ratio between magnetic flux and the magnetomotive force induced by it [3], [23].

$$P = \frac{\phi}{F} \implies \frac{B * A}{H * d} \implies \frac{\mu * A}{d} \tag{2.8}$$

The reluctance is the measure of resistance to flux flow in a material. It is analogous to the electrical resistance in a magnetic circuit and can be modeled as the reciprocal of permeance [3], [42]. The mathematical equation describing this property is as mentioned in Equation 2.9.

$$R = \frac{1}{P} \implies \frac{d}{\mu * A} \tag{2.9}$$

The area of the cross-section perpendicular to the flux flow, highlighted in green color in Figure 2.11a, is the effective cross-section through which the flux lines flow, represented by "A." The "d" denotes the length of the magnetic field line through the circuit.

The magnetic field distribution at critical points is investigated by applying the circuit theory and solving for the flux density to the different parts [43], [44], [48].

2.9.1 Flux Density Distribution in Air Gap

In EMs, a gap exists between the stator and the rotor. This gap contains air, which is a non-magnetic material. For the machine to perform efficiently, the flux needs to get across the air gap and interact with the flux produced by the coils that generate the force required to cause the torque [13].

The flux lines passing through the air gap are distorted due to magnetic saturation, slot geometry, the permeability of the material, and the combined effect of winding MMF [13]. This phenomenon is called fringing.

Flux lines prefer the path of higher permeability. However, since the air in the air gap between the stator and rotor core has a very low permeability, they spread out near the edges, causing the fringing effect. Additionally, the stator slots hold the winding and are usually semi-closed or open. These slots interrupt the continuity of the flux flow from the rotor, causing the flux lines to spread and distort [3].

The fringing effect causes a reduction in magnetic flux within the air gap of EMs, effectively increasing the air gap length, decreasing the overall torque output [49]. The fringing effect can be accounted for by applying the Carter coefficient to determine the effective air gap length.

While the fringing effect cannot be eliminated, it can be reduced by various design approaches, such as wider tooth design, incorporating a flux barrier in the air gap, laminating the stator and rotor, and using high-permeability materials.

2.9.2 Importance of Investigating Saturation Point

The position of the magnet in the rotor is an essential parameter that defines the pole cap and bridge dimensions [31]. It determines both the magnet's distance from the air gap and the amount of flux that flows into the air gap during its operation [11], [13]. The farther the magnet from the air gap, the lesser the flux that enters. Since flux lines tend to flow in the path of higher permeability, this increases flux leakage into the bridge, ultimately reducing the machine's efficiency. Therefore, the bridge is saturated to remain less involved in the flux movement and prevents leakage [11].

2.9.3 Back-Electromotive Force

When the rotor rotates due to the interaction of the magnetic fields between the stator coils and the rotor, an electromotive force is generated in the coils [24]. This is called the Back-Electromotive Force (BEMF), which is induced by the changing magnetic field and is given by Farraday's law [13].

The BEMF is proportional to the angular speed of the rotor. When the machine is not rotating, there is no changing magnetic field, and BEMF is zero. At low speed, the machine draws maximum current as the driving voltage is maximum. However, as the speed increases, the BEMF increases. This counters the supplied voltage, reducing the net driving voltage and current.

The stator winding configuration also determines the shape of the BEMF waveform. As it is caused by the varying magnetic field and its influence on the stator coils. A concentrated winding generates a trapezoidal BEMF as the coils are arranged on a single tooth. The peaks occur only when magnets are aligned with these coils. On the other hand, since they are distributed over many teeth, the BEMF tends to be more sinusoidal. This is advantageous, as having a sinusoidal waveform eliminates irregularities such as voltage surges or spikes that can harm electronic devices.

2.10 Electromagnetic Torque

In an IPMSM, the rotor magnets experience a couple force due to the magnetic energy present across the air gap. These forces, which are electromagnetic in nature, induce rotational motion in the rotor. This rotation generates torque, commonly referred to as

electromagnetic torque.

The torque generated is essential for driving mechanical loads connected to the machine shafts. The primary force experienced by the magnet when placed in the magnetic field generated by the stator winding is either attraction or repulsion. This force causes the rotor to rotate resulting in electromagnetic torque.

The structure of an IPMSM is such that the magnets are placed within the rotor, creating magnetic saliency [50], that is, the variation of the reluctance along the rotor's axis. This saliency produces additional reluctance torque which combines with magnetic torque to increase the total torque output.

Due to the attractive and repulsive forces on magnets by the field generated by the stator winding and reluctance force, equal and opposite couple forces act on the magnets, generating a rotational torque on the rotor. In an EM, the electromagnetic torque and power output are directly affected by the air gap flux density. Higher flux density in the air gap increases magnetic interaction in the air gap, thereby increasing the torque output and consequently, power output at a given speed.

Electric loading is defined as the total current around the stator per unit length. It determines the current-induced magnetic field in the stator winding. Electric loading directly influences the flux density in the air gap, which increases with an increase in electric loading subsequently increasing torque and power.

BEMF opposes the applied voltage in an EM, reducing the net voltage driving the current through the windings. Since electromagnetic torque is proportional to electric loading, increased BEMF at higher speeds lowers the current, resulting in a reduction in torque. This limits torque generation at high speeds.

2.10.1 Cogging Torque and Torque Ripple

Cogging is an undesirable component caused by the magnet, which produces attractive forces on all the magnetic materials. This attraction force locks the rotor position with respect to the stator. The torque required to overcome this position dependency or for the rotor to advance from the locked position is the cogging torque.

Cogging torque results in uneven torque output, and this variation in the torque output is known as the torque ripple [51]. Torque ripple and cogging torque go hand in hand; that is, the higher the cogging torque, the higher the torque ripple will be [51].

The cogging torque is significant since IPMSM has a magnet in its rotor [52]. It depends on various factors like the magnet's strength, field strength, the combination of slot and pole, and tooth structure.

The slot-pole combination in IPMSM affects torque by influencing harmonics, cogging torque and ripple. The optimized slot-pole ratio reduces the undesirable cogging between the stator and the rotor, reducing the torque ripple. A good slot-pole ratio also reduces radial forces, improving efficiency and overall torque output. A good slot-pole ratio should

be such that the least common multiple of the slot-pole number should be higher [26].

The stator winding pattern, such as distributed or concentrated winding, affects the magnetic field distribution, thereby affecting the torque generated. The concentrated winding generates high torque but has lower efficiency at higher speeds due to harmonics [12]. The distributed winding produces more sinusoidal Back-EMF, reducing losses in stator and rotor [12], [13]. Poor winding design can lead to torque ripple, causing fluctuations in torque output, and reducing the smoothness of the machine.

2.11 Electromagnetic Power

Electromagnetic power in an IPMSM refers to the power generated by the magnetic field energy in the air gap. This power results from converting electrical power supplied to the stator windings into mechanical power, ultimately driving the machine's rotor.

When three-phase AC flows through the stator windings, it creates a rotating magnetic field. This rotating magnetic field has a frequency determined by the input AC signal and generates a rotating magnetic flux. The speed of this rotating field called the synchronous speed, depends on the frequency of the AC supply and the number of poles in the motor. This rotating field provides the basis for electromagnetic power generation.

The rotor of an IPMSM contains permanent magnets arranged in a specific geometry, creating a steady magnetic field within the rotor. The stator's rotating magnetic field interacts with the rotor's permanent magnets, causing a magnetic force on the rotor. The alignment and synchronization between the stator and rotor magnetic field produce a continuous rotational force on the rotor, allowing it to follow the synchronous speed of the stator field without slipping.

2.11.1 Losses in IPMSM

Losses in an IPMSM can be divided into several categories, each impacting the machine's efficiency and performance. Understanding these losses is crucial for improving machine design and optimizing energy usage.

The difference in power the machine pulls from the battery systems and the power produced at the machine shaft gives the total loss. These losses happen at different parts of the machine, namely, copper losses in the winding, hysteresis, and eddy current losses at the stator and rotor core.

Copper losses happen due to the resistance of the winding when current flows through it, resulting in power being lost in the form of heat. As the current increases, the copper loss increases exponentially. Consequently, at lower operating speeds, where the torque output is higher, these losses become particularly significant.

Hysteresis losses occur due to the changing magnetic field polarity, causing the stator core to undergo repeated magnetization and demagnetization. Eddy current losses occur in the core and the magnets as they are subjected or exposed to the time-varying magnetic

field, which induces current and increases the heat.

3

Methods

3.1 Design Workflow

The computational tool was developed using Python. The tool's purpose was to parameterize the machine sizing parameters based on machine requirements enhancing the initial design phase. The implemented approach aimed to establish a quick and easy method to design an EM.

Figure 3.1 describes the design workflow of the computational tool. The tool was designed to generate initial machine sizing parameters by considering the fixed variables, dependent variables, material constants, and adjustable variables. The fixed variables were the decision-making variables that defined the input to the tool based on the machine's requirements. The material properties were specified and were not changed throughout the design. The tool offered flexibility to a designer to choose and vary the adjustable variables to achieve the machine's performance.

The dependent variables obtained from fixed, material, and adjustable variables for machine sizing parameters were used as input and output. The preliminary designs of key parameters like overall machine dimension, winding, stator slot and tooth dimensions, and magnet dimensions were subjected to electromagnetic analysis. We evaluated flux and flux density at critical regions, assessed magnet demagnetization under winding field effects, optimized magnet dimensions and calculated electromagnetic torque, power, back-EMF, and flux linkage. The results of this analysis were compared with predefined machine requirements. The developed tool iteratively optimizes the parameters to achieve improved output, ensuring alignment with performance expectations. The sizing parameters can be refined for precision using FEM solvers.

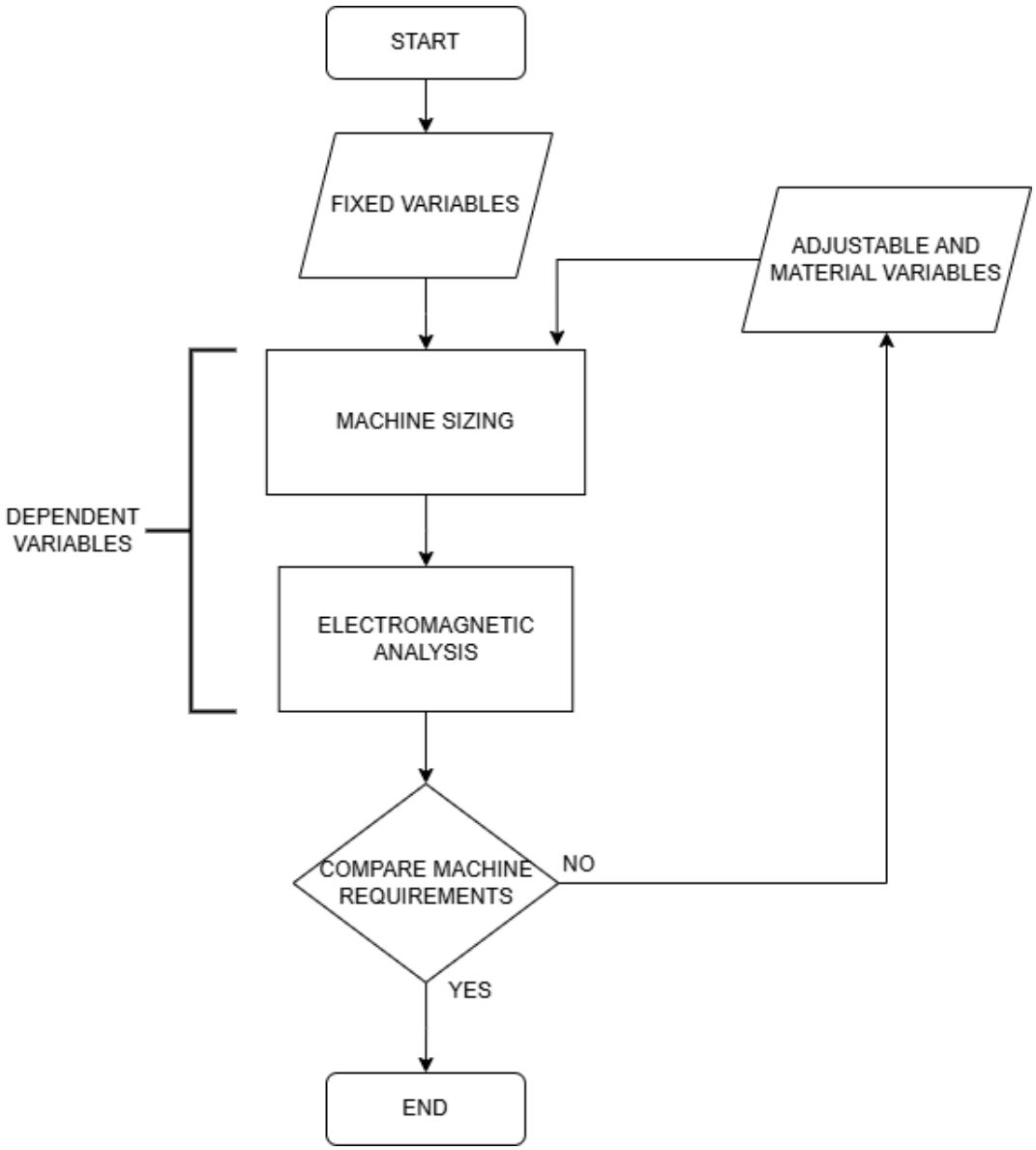

Figure 3.1: Illustration of Design Workflow

3.2 Assumptions

To simplify the mathematical model and establish analytical equations to investigate the sizing of EMs, certain assumptions and boundary conditions were employed [3], [53].

1 The PM chosen was Neodymium magnets with parallel magnetization.

2 BEMF voltage waveform was sinusoidal.

3 Infinite permeability in the iron core, hence the magnetic saturation was being neglected.

4 The stator and rotor cross-section area flux distribution were assumed to be uniform.

5 The fringing effect near the slots was neglected to simplify the air gap geometry.

6 The non-linear behavior and the temperature effects increase the complexity and make it hard to be captured by an analytical method. Hence, the temperature effects were not considered while modeling and the material properties were modeled for a specific temperature of around 20 °C.

3.3 Overall Motor Sizing

The overall machine sizing aimed to determine the rotor and stator volumes necessary to achieve the required torque and power [3]. This established a geometrical constraint that guided the sizing of the machine's components [26].

3.3.1 Estimation of Volume and Dimensions of Rotor by TRV Method

Based on the torque requirement and the TRV selected from Table 2.1, the rotor's volume was calculated using Equation 3.1 [26].

$$TRV = \frac{RatedTorque}{V_{rotor}} \implies V_{rotor} = \frac{RatedTorque}{TRV} \tag{3.1}$$

Since the rotor is cylindrical, the volume of the rotor was established using Equation 3.2.

$$V_{Rotor} = \frac{\pi * D_{rotor}^2 * L_{stk}}{4} \tag{3.2}$$

The choice of aspect ratio was pre-determined based on the criteria elaborated in Section 2.4. Equation 3.3 related the pole-pitch to the stack length.

$$AspectRatio = \frac{L_{stk}}{\tau_p} \tag{3.3}$$

where $\tau_p = \frac{\pi * D_{rotor}}{p}$ [m] is the pole pitch.

The diameter of the rotor was calculated by substituting and rearranging Equation 3.2 and Equation 3.3 in Equation 3.1.

$$D_{rotor} = \sqrt[3]{\frac{4 * RatedTorque * p}{TRV * AspectRatio * \pi^2}} \tag{3.4}$$

3.3.2 Estimation of Stator Dimensions

First, the rotor volume was fixed using the above expressions. Based on the calculated rotor diameter, the split ratio was used to calculate the stator's outer diameter. This is shown in Equation 3.5 [25].

$$SplitRatio = \frac{D_{rotor}}{D_{OuterStator}} \tag{3.5}$$

The stator's inner diameter was also calculated using the rotor's outer diameter. Since the air gap thickness was predefined, Equation 3.6 was used to determine it [11], [13], [31].

$$D_{InnerStator} = D_{rotor} + 2 * d_g \tag{3.6}$$

3.3.3 Overall Dimensioning Parameter Estimations

Figure 3.2 describes the schematic representation to develop the overall sizing parameters of the machine, which indicates the input, output, and pre-defined variables. The dependent variables are the output, which includes: rotor outer diameter (in m), stack length (in m), stator inner diameter (in m), and stator outer diameter (in m).

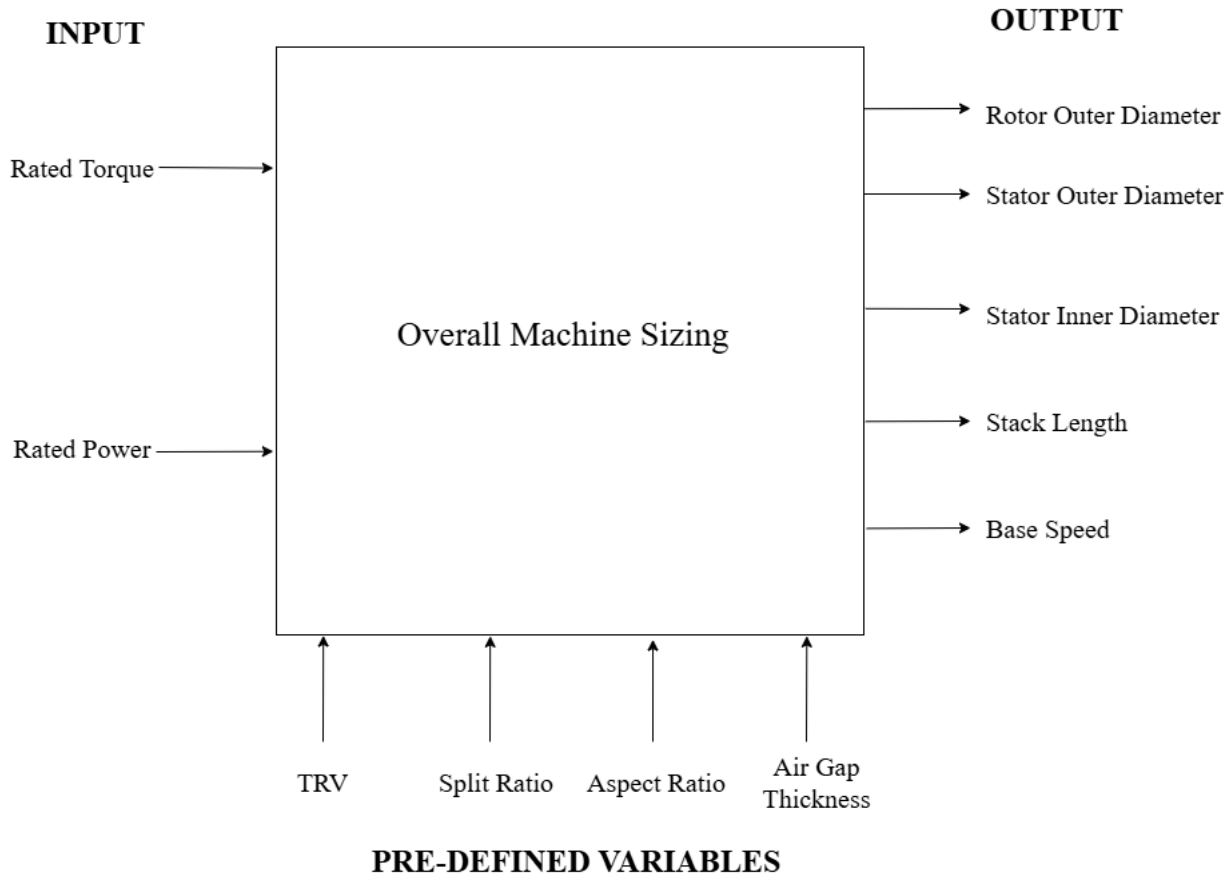

Figure 3.2: Schematic Representation Describing Overall Sizing of IPMSM

The torque (in Nm) and power (in W) are the fixed variables that define the requirements of the machines. These parameters are the inputs to the computational tool and are the decision variables for overall machine sizing.

The TRV (in $\frac{Nm}{m^3}$), aspect ratio, split ratio, and air gap thickness (in m) are the constraints or adjustable variables that are required to meet the objective function.

The selection of adjustable variables followed conditions or a range of values as follows:

1 The TRV was selected from Table 2.1 based on machine application and volume limitations.

2 The aspect ratio was bound within 0.5 to 2, and the choice of value was based on torque and speed capabilities.

3 The rotors of an IPMSM are internal, and hence, the split ratio ranged between 0.6 and 0.8.

4 Air gap thickness varied between 0.5 mm and 1 mm.

3.4 Stator Profile Sizing

This section examines the winding design and the stator profile sizing. It also elaborates on the Python script by describing its input, output, and preset variables that are essential for the design.

3.4.1 Stator Winding Parameters

This study considered distributed, full-pitch winding that produces back EMF which is sinusoidal in nature. The turns per phase refers to the number of turns for each phase winding around the stator core. It depends on the fundamental frequency (in Hz), DC bus voltage (in V), and air gap flux (in Wb). The turns per phase was estimated using Equation 3.8.

$$V_{phaseRMS} = \frac{V_{DC}}{\sqrt{3}} \tag{3.7}$$

$$T_{ph} = \frac{V_{phaseRMS} * \sqrt{2}}{\pi * K_w * \phi_g * f} \tag{3.8}$$

where T_{ph} is turns per phase, K_w is the winding factor, ϕ_g is the air gap flux (in Wb) and f is the fundamental frequency (in Hz).

Coils per pole represent the number of coils of a specific phase for one pole as given in Equation 3.9

$$N_{cp} = \frac{N_{ss}}{m * N_p} \tag{3.9}$$

where N_{cp} represents coils per phase, N_{ss} is the number of stator slots, m is the number of phases, and N_p is the number of poles.

Turns per coil refers to the number of times the wire is wound within a coil of a stator core. Each coil is made of multiple turns as given by Equation 3.10

$$N_{tc} = \frac{n * T_{ph}}{N_{cp} * N_p} \tag{3.10}$$

where n is the number of parallel paths.

The current flowing through the conductors is known as phase current (in A) and was estimated by the power (in W) equation represented in Equation 3.11

$$I_{phaseRMS} = \frac{Power}{3 * EMF * \cos\phi} \tag{3.11}$$

where $\cos\phi$ is the power factor of the machine.

Current density refers to the electric current flowing per unit cross-section of the conductor. For an EM, the current density value ranges from 6-11 $\frac{A}{mm^2}$. Using the current density and phase current values, the area of the conductor was estimated using Equation 3.12

$$A_C = \frac{I_{phaseRMS}}{J} \tag{3.12}$$

where J is the current density of the conductors (in $\frac{A}{m^2}$).

3.4.2 Stator Tooth Dimensions

The number of stator teeth refers to the total number of teeth present along the inner circumference of the stator. The number of teeth depends on the number of poles in the rotor as given by Equation 3.13

$$N_{ss} = N_p * m * q \tag{3.13}$$

where q is the number of slots per pole per phase. The q was selected based on the criteria that slot pitch should be in the range of 15-25 mm. This is because the slot must provide sufficient area to accommodate the winding, while the tooth must be adequately wide to avoid magnetic saturation under the applied field.

The stator tooth design is constrained by the maximum permissible magnetic flux. As mentioned in Section 2.2, the tooth should be wide enough to let the magnetic flux flow through it without reaching the point of saturation. The width of the tooth at the top was estimated using Equation 3.14

$$W_{tht} = \frac{N_p * B_{gPeak} * W_g}{N_{ss} * B_{tpk}} \tag{3.14}$$

where B_{gPeak} is the peak air gap flux density (in T), and B_{tpk} is the maximum permissible flux density (in T) of the tooth beyond which the tooth saturates for the stator material.

As the tooth is notched, the tooth width at the air gap is wider than the width at the yoke end. The tooth width at the air gap was estimated using Equation 3.15.

$$W_{thb} = W_{tht} * 1.2 \tag{3.15}$$

The stator tooth pitch is the distance between the center point of one tooth to the center of the consecutive tooth as given by Equation 3.16

$$\tau_s = \frac{\pi * D_{InnerStator}}{N_{ss}} \tag{3.16}$$

3.4.3 Stator Slot Dimensions

The stator slot should accommodate all the winding as mentioned in Section 2.2. The slot area was estimated using Equation 3.17.

$$A_s = \frac{N_{tc} * A_c}{K_f} \tag{3.17}$$

where K_f is the fill factor.

The width of the slot at the bottom was estimated using Equation 3.18

$$W_{sb} = \tau_s - W_{thb} \tag{3.18}$$

The height of the slot was estimated using the area and width of the slot by Equation 3.19

$$H_s = \frac{A_s}{1.1 * W_{sb}} \tag{3.19}$$

The stator yoke is the outer structural part of the stator. It is a hollow cylindrical structure that provides mechanical support and serves as the path for the magnetic field.

The yoke height was estimated using the stator outer boundaries and the slot height using Equation 3.20.

$$H_{ys} = \frac{D_{OutStator} - (D_{InStator} + 2 * H_s)}{2} \tag{3.20}$$

3.4.4 Investigation of Fringing Effect

The fringing effect refers to the bending of flux lines along the edges of the stator tooth caused by changes in the permeability of the medium and the presence of stator slots, as explained in Section 2.9.1. This effect was accounted for by a constant known as the Carter Coefficient. The Carter Coefficient depends on the stator tooth and slot profile and was estimated by Equation 3.22.

$$K_{th} = \frac{W_{thb}}{\tau_s} \tag{3.21}$$

$$K_c = \frac{K_{th} * (4.44 * d_g + 0.5 * W_{sb})}{K_{th} * (4.44 * d_g + 0.5 * W_{sb}) - W_{sb}^2} \tag{3.22}$$

After considering the fringing effect, the effective air gap thickness was calculated using Equation 3.23.

$$d_{eg} = K_c * d_g \tag{3.23}$$

3.4.5 Stator Sizing Parameter Estimations

Figure 3.3 is a schematic representation of the winding and stator parameters of the machine. The focus is on sizing the stator slot and tooth, and design winding. Hence, the dependent variables are turns per phase T_{ph}, turns per coil N_{cp}, area of slot A_s (inm^2), width of slot W_{sb} (in m), height of slot H_s (in m), width of tooth W_{thb} (in m), Carter Coefficient K_c and effective air gap thickness D_{eg} (in m).

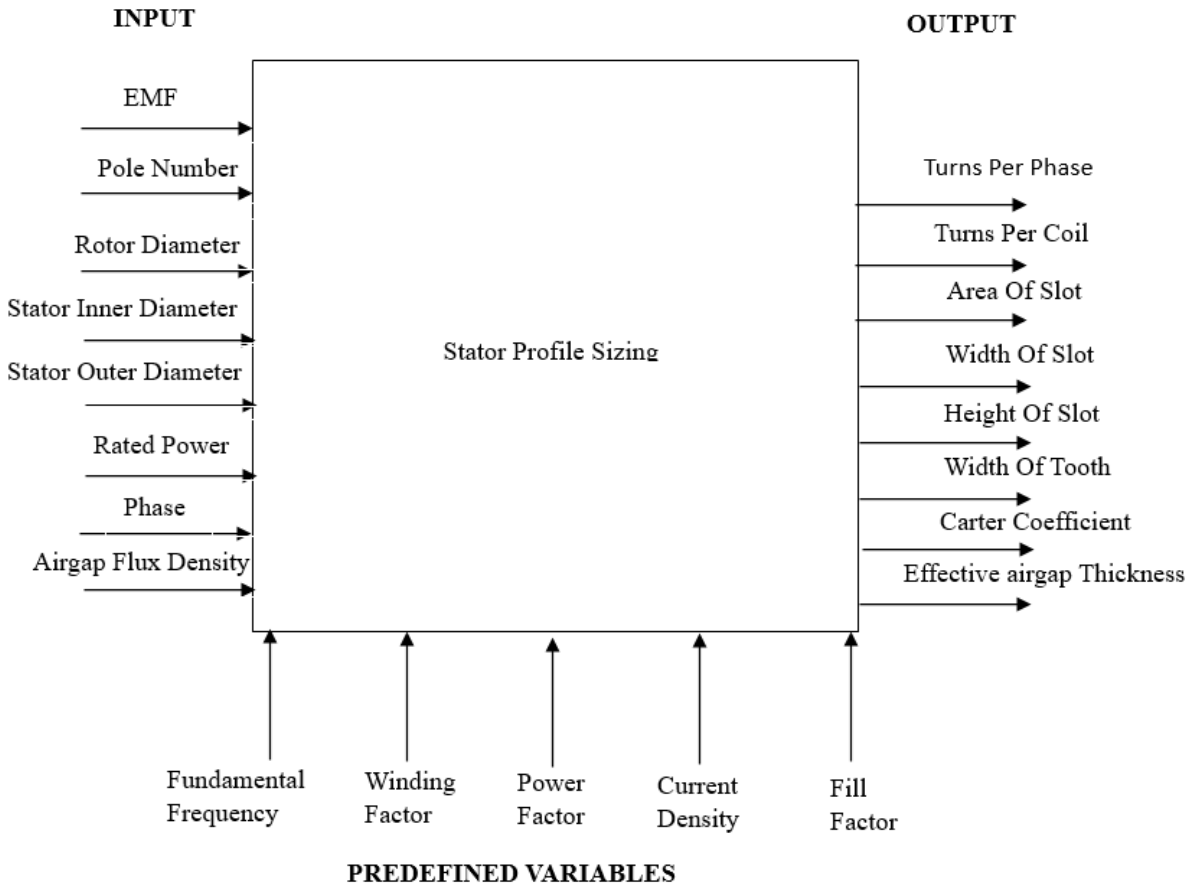

Figure 3.3: Flowchart Describing the Algorithm of Stator Sizing of IPMSM

The inputs to estimate these dependent variables are the output from the overall sizing and rotor profile sizing, which gives the overall stator dimensions.

The DC voltage (in V), rated power (in W), winding factor K_W, fundamental frequency f (in Hz) and number of phases are fixed variables that help estimate winding parameters.

The adjustable variables are Power Factor, Current density J, and Fill Factor K_f.

1 The power factor of the machine ranges between 0.7 and 0.98. It depends on the type of machine configuration.

2 Current density J ($in \frac{A}{mm^2}$) refers to the electric current flowing per unit cross-section of the conductor. For an EM, the current density value ranges from 6-11 $\frac{A}{mm^2}$

3 The Fill Factor K_f is the ratio of cross-sectional area occupied by the conductor in the slot to the total cross-sectional area of the slot. The value of the fill factor usually ranges from 0.3 to 0.7.

3.5 Rotor and Permanent Magnet Sizing

This section focuses on sizing and positioning the magnet in the rotor core. It also elaborates on the Python script by describing its input, output, and preset variables essential for the computations.

3.5.1 Base Speed Estimation

The rotor's design is based on the base speed. Equation 3.24 investigated the base speed for the rated torque (in Nm) and rated power (in W) [2].

$$BaseSpeed = \frac{RatedPower}{RatedTorque} \tag{3.24}$$

The estimated base speed also plays a role in deciding fundamental frequency and the number of poles needed in the rotor for the required performance [11], [31].

3.5.2 Pole Selection

The number of poles was initially calculated using Equation 3.25. It was constrained by the base speed (in RPM) and the fundamental frequency (in Hz) [26].

$$p = \frac{120 * f}{BaseSpeed(inRPM)} \tag{3.25}$$

3.5.3 Pole-Pitch and Pole-Arc

As described in Section 2.2, pole-pitch is the arc length between the centers of two adjacent magnets on the rotor lamination. The pole-pitch constrains the size of the magnet and the rotor diameter. This was calculated using Equation 3.26 [22].

$$\tau_p = \frac{\pi * D_{rotor}}{p} \tag{3.26}$$

where p = Number of poles and D_{rotor} is the diameter of the rotor (in m).

The pole-arc subtends the magnet within a pole and was calculated using Equation 3.27 [22].

$$\tau_m = \alpha_p * \tau_p \tag{3.27}$$

where τ_m is the pole arc, and τ_p is the pole pitch [19], [20]. The ratio of pole-arc to pole-pitch, also called the embrace angle, referred to as α_p in Equation 3.27 has been deduced between 0.6 and 0.85 [19], [20], [22] for optimal torque performance with reduced cogging torque and torque ripple and also minimizing the back-EMF.

3.5.4 Magnet Sizing

The magnet is the most expensive component of the machine to manufacture [16]. Hence the geometry and volume of the magnet are key to the machine's cost.

A balance between performance and cost needs to be an important criterion for selecting and sizing the magnets [11], [13].

3.5.4.1 Magnet Width Estimation

Figure 3.4 describes a magnet placed in a pole of the rotor such that the magnet's center coincides with the chord AB's center. The arc AB is the pole-pitch (τ_p), and the arc CD is the pole-arc (τ_m). The distance from the pole cap to the magnet (d_{pc}) is defined as the pole-cap length.

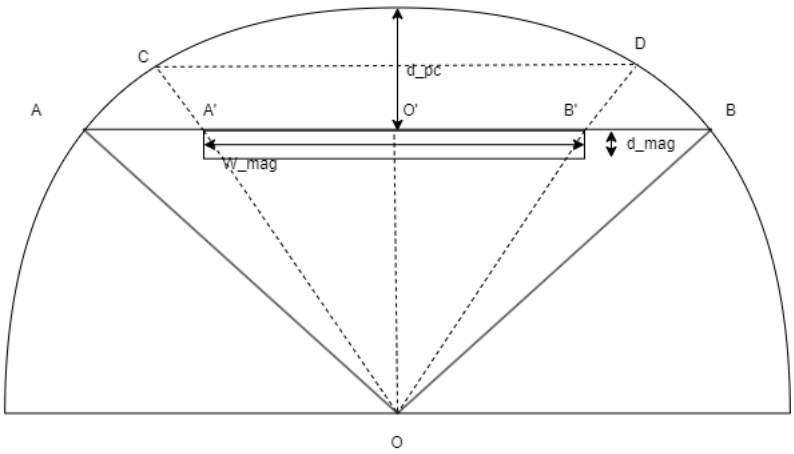

Figure 3.4: Representation of Pole Cap Length and Magnet Width

The pole arc was estimated in Equation 3.27 and the angle subtended by the arc was calculated using the arc length formula as given in Equation 3.28

$$\theta_m = \frac{\tau_m * 360}{\pi * D_{rotor}} \tag{3.28}$$

The angle (in degrees) subtended by the pole-pitch was calculated using Equation 3.29

$$\theta_p = \frac{360}{p} \tag{3.29}$$

The width of the magnet (W_m) (in m) was calculated from the Δ AO'O using the trigonometric relations. From the Δ AO'O, the Equation 3.30 was deduced.

$$\sin\frac{\theta_p}{2} = \frac{AO'}{AO} = \frac{AB}{D_{rotor}} \tag{3.30}$$

Using Equation 3.30, the chord AB was deduced as in Equation 3.31

$$AB = D_{rotor} * \sin\frac{\theta_p}{2} \tag{3.31}$$

Assuming that ratios at all points between AB and CD were maintained, the width of the magnet was estimated by the following Equation 3.32.

$$W_{mag} = \alpha_p * D_{rotor} * \sin\frac{\theta_p}{2} \tag{3.32}$$

3.5.4.2 Magnet Thickness Estimation

Analogous to an electric circuit, a magnetic field generates magnetic potential through the circuit shown in Figure 3.5 [47].

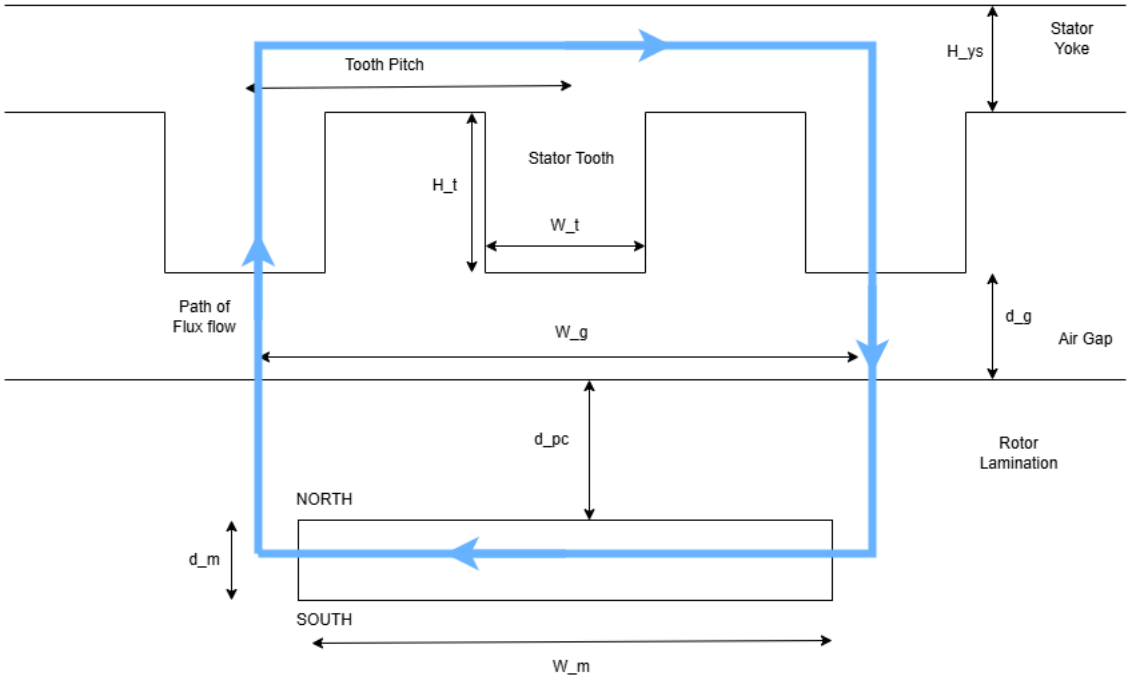

Figure 3.5: Representation of Flow of Flux Lines in the Open Magnetic Circuit

The magnetic potential across individual parts of the machine in an open-circuit model was estimated using Ampere's law and is given by Equation 3.33 [22].

$$\int H * dl = 0 \tag{3.33}$$

where H is the magnetic field intensity (in $\frac{A}{m}$) and dl is the length of the magnetic circuit (in m).

Equation 3.34 was deduced by expanding Equation 3.33 to the circuit in Figure 3.5.

$$H_{mag} * d_{mag} + H_{rot} * d_{pc} + H_g * d_g + H_t * d_t + H_{ys} * d_{ys} = 0 \tag{3.34}$$

The relation of flux density and magnetic field intensity as introduced in Section 2.5 is given by Equation 3.35.

$$B = \mu * H \tag{3.35}$$

where μ is the relative permeability of the different parts in the magnetic circuit.

Equation 3.36 was derived from Equations 3.34 and 3.35.

$$\frac{B_{mag} - B_r}{\mu_0 * \mu_m} * d_{mag} + \frac{B_g}{\mu_0} * d_g + \frac{B_t}{\mu_0 * \mu_s} * d_t + \frac{B_{ys}}{\mu_0 * \mu_s} * d_{ys} = 0 \tag{3.36}$$

under the assumption that the rotor is infinitely permeable and the flux produced by the magnet flows through the rotor core to the air gap [13]. The flux produced by the magnet is equal to the flux in the rotor core as shown in Equation 3.37 implying there is no flux leakage between the magnet and the rotor core.

$$\phi_{rot} = \phi_{mag} \implies B_{rot} = B_{mag} \tag{3.37}$$

However, the flux is then divided into two parts. Some flux is leaked into the bridge section of the rotor [13]. The remaining flux flows into the air gap through the magnetic circuit path. This leakage factor calculates the amount of flux inducting across the air gap.

From Equation 3.37 the flux flowing into the air gap is given Equation 3.38.

$$\phi_g = \phi_{rot} * K_l \implies B_g = \frac{B_{rot} * A_{rot}}{A_g} * K_l \tag{3.38}$$

where the K_l is the flux leakage factor that represents the percentage of the flux that enters the air gap.

Since there are $\frac{N_t}{N_p}$ number of teeth per pole, the flux gets equally divided among them [31]. Hence, the flux flowing through the stator tooth and yoke is given by Equations 3.39 and 3.40, respectively.

$$\phi_g = \frac{N_t}{N_p} * \phi_t \implies B_t = \frac{N_p}{N_t} * B_g * \frac{A_g}{A_t} \tag{3.39}$$

$$\phi_{ys} = \frac{N_t}{N_p} * \phi_t \implies B_{ys} = \frac{N_t}{N_p} * B_t * \frac{A_t}{A_{ys}} \tag{3.40}$$

After evaluating the flux densities in individual parts of the magnetic circuit, the thickness of the magnet was estimated by rearranging the terms in Equation 3.36. Ultimately, the thickness of the magnet was calculated using Equation 3.41.

$$d_{mag} = (-(\frac{B_{rot}}{\mu_0 * \mu_{rot}} * d_{pc} + \frac{B_g}{\mu_0} * d_g + \frac{B_t}{\mu_0 * \mu_s} * d_t + \frac{B_{ys}}{\mu_0 * \mu_s} * d_{ys})) * \frac{\mu_0 * \mu_m}{B_{mag} - B_r} \tag{3.41}$$

3.5.5 Magnet Positioning

As mentioned in Section 3.5.4.1, the magnet is placed on chord AB initially. In Δ A'O'O in Figure 3.4, the OO' was calculated using the trigonometric ratio of the ⟨ A'OO' ($\frac{\theta_m}{2}$). This is given in the Equation 3.42.

$$\tan(\frac{\theta_m}{2}) = \frac{W_{mag}}{2 * OO'} \implies OO' = \frac{W_{mag}}{2 * \tan(\frac{\theta_m}{2})} \tag{3.42}$$

The pole cap thickness was evaluated from the Equation 3.43.

$$d_{pc} = \frac{D_{rotor}}{2} - OO' \implies d_{pc} = \frac{D_{rotor}}{2} - \frac{W_{mag}}{2 * \tan(\frac{\theta_m}{2})} \tag{3.43}$$

In Figure 3.4, two triangles were drawn above the magnet, relating the pole cap and bridge thickness. The triangles were constructed by drawing perpendicular lines from the pole cap to the magnet and point C to the magnet forming lines O"O' and CC'. These triangles are similar and shown in Figure 3.6.

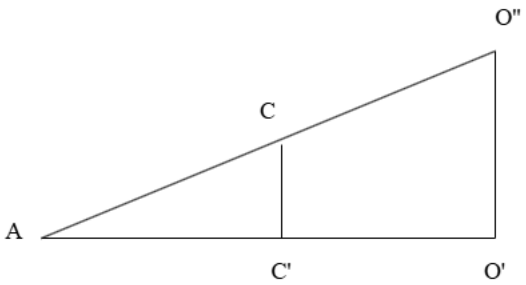

Figure 3.6: Representation of Triangles Relating Pole Cap Thickness to Bridge Thickness

By similar triangle principles the Equation 3.44 was deduced.

$$\frac{CC'}{O"O'} = \frac{AC}{AO"} \tag{3.44}$$

since the magnet is very close to the circumference of the rotor, $AC = \frac{\tau_p - \tau_m}{2}$ and $AO" = \frac{\tau_p}{2}$. The perpendicular lines CC' and O"O' represent the bridge thickness (d_{bridge}) and pole cap thickness (d_{pc}) respectively.

Therefore, the bridge thickness was calculated by Equation 3.45.

$$\frac{d_{bridge}}{d_{pc}} = \frac{\frac{\tau_p - \tau_m}{2}}{\frac{\tau_p}{2}} \implies d_{bridge} = \frac{\tau_p - \tau_m}{\tau_p} * d_{pc} \tag{3.45}$$

3.5.6 Rotor Sizing Parameter Estimations

The schematic representation in Figure 3.7 illustrates the variable requirement for the rotor profile sizing. This focuses on calculating the magnet's dimensions, its position, and the volume available in the rotor pole for the magnet. Hence, the dependent variables include the number of poles N_p, Width of the magnet (in m), thickness of the magnet (in

m), pole cap thickness (in m), bridge thickness (in m), pole pitch (in m), pole arc (in m), optimized width of magnet (in m) and optimized thickness of the magnet (in m).

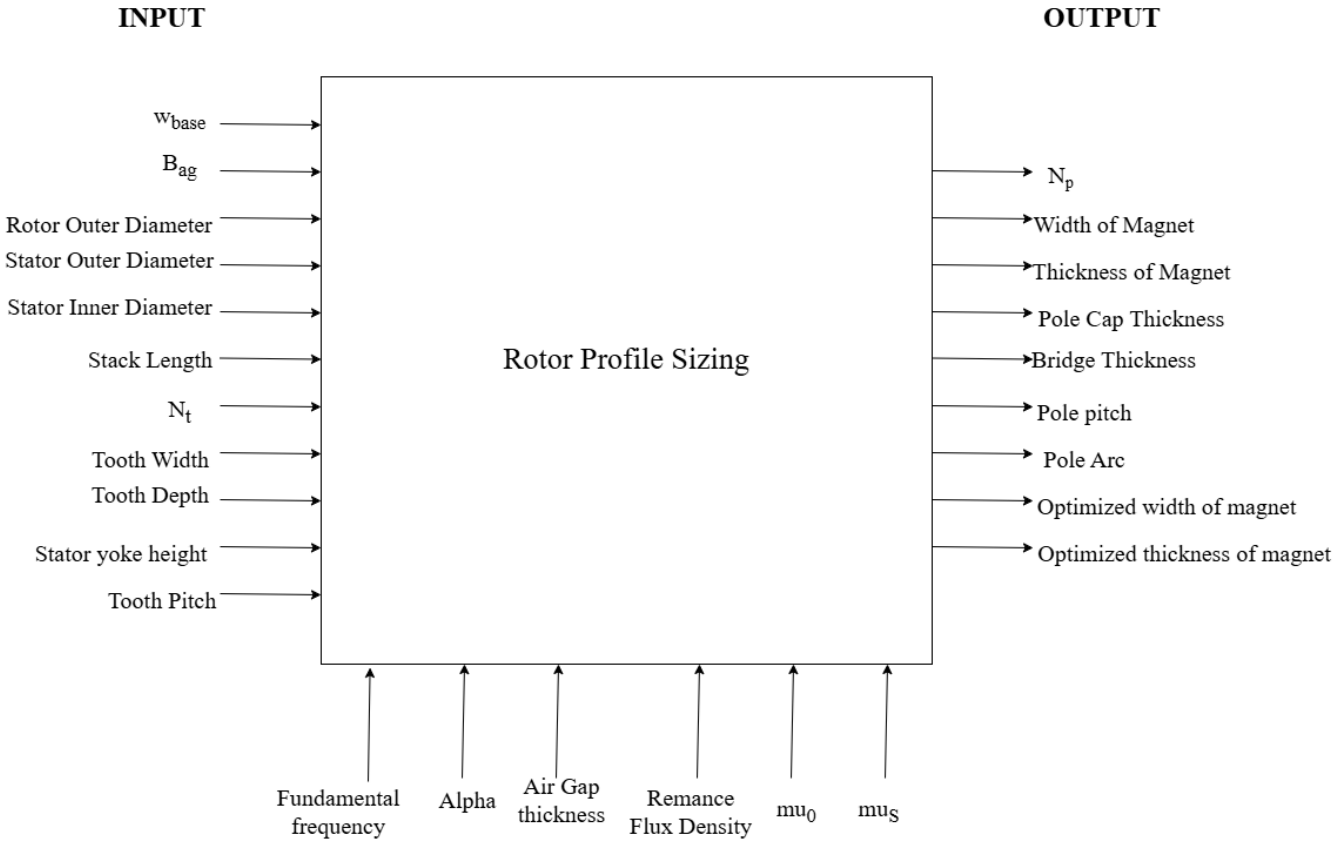

Figure 3.7: Schematic Representation Describing Rotor Profile Sizing of IPMSM

The inputs to these calculations were the dependent variables from overall machine sizing and stator profile sizing as they defined the available rotor and machine volume. The fundamental frequency (in Hz) that defined the number of poles required for the rated speed was a fixed variable defined for a power source.

The material constants and adjustable variables included were remanence flux density (in T), mu_0 (in H/m), mu_s, alpha, air gap thickness (in m), and B_{ag} (in T) as follows:

1 The remanence flux density is dependent on the selected magnet type and grade; for example, N35 has 1.21 T as its remanence flux density [16].

2 The permeability constant of vacuum mu_0 is 0.000001256 $\frac{H}{m}$.

3 The relative permeability of the rotor (mu_s) depends on the material chosen for the rotor; for example, electrical steel has a value of 4000.

4 The alpha value can be chosen by the designer and can be varied. For optimum machine performance, the value ranges between 0.6 and 0.8.

5 The air gap thickness ranges between 0.5 mm and 1 mm. B_{ag} can be chosen between 0.6 and 0.8 for PMSM [12].

3.6 Modelling Operating Point of Magnet

Considering the linear properties of the Neodymium magnets (NdFeB) [16], the BH characteristics of the magnet are curve fit using tools from the Python library with data from manufacturer specifications at temperature of 20 ° C [32]. As discussed in Section 2.7, the intersection of the BH curve and load line defines the OP [30]. The load line was investigated by calculating the P_c for the open-loop condition of the magnetic circuit with the air gap [3], [26].

The P_c was derived by studying the magnetic flux distribution and the magnetic potential across the magnet and the air gap [3], [30]. First, the line integral of the magnetic field in the open-loop was estimated using Equation 3.46 [3], [30].

$$H_g * d_g + H_d * d_m = 0 \implies H_g = \frac{-H_d * d_m}{d_g} \tag{3.46}$$

where H_g and H_d are the magnetic field intensities (in $\frac{A}{m}$) in the air gap and magnet and d_g and d_m are the thickness of the air gap and magnet (in m), respectively.

The flux flows into the air gap through the pole cap region and the flux density at the air gap were deduced from Equation 3.37 and Equation 3.38 to form Equation 3.47.

$$B_g = B_d * C_\phi * K_l \tag{3.47}$$

The flux density in the air gap is proportional to its field intensity and represented by Equation 3.48 [13], [30].

$$B_g = \mu_0 * H_g \tag{3.48}$$

The P_c was obtained by substituting Equations 3.46 and 3.47 in Equation 3.48 for B_g and H_g.

In an open-circuit condition when there is no current flowing through the stator windings and an ideal case of no flux leakage ($K_l = 1$), the P_c is given by Equation 3.49.

$$P_c = \frac{-B_d}{\mu_0 * H_d} = \frac{d_m}{d_g * C_\phi} \tag{3.49}$$

At loaded conditions, the windings generate an opposing demagnetizing field that reduces the contribution of magnet flux in the air gap. This excitation leads to demagnetizing effects, which are described in Section 2.7.2. This was implemented to calculate the new flux density in the air gap by the magnet using Equation 3.50.

$$B_d = -\mu_0 * P_c * H_d - \frac{N * I}{d} \tag{3.50}$$

Equations 2.1 and 3.50 were solved by using the simultaneous approach to calculate the operating points.

3.7 Electromagnetic Analysis

The magnetic circuit describes the closed path of the flux flow [29]. Figure 3.8 illustrates the MEC overlapped on the rotor and stator, a blue color code. Considering one half of the magnet, the reluctances of different parts are modeled.

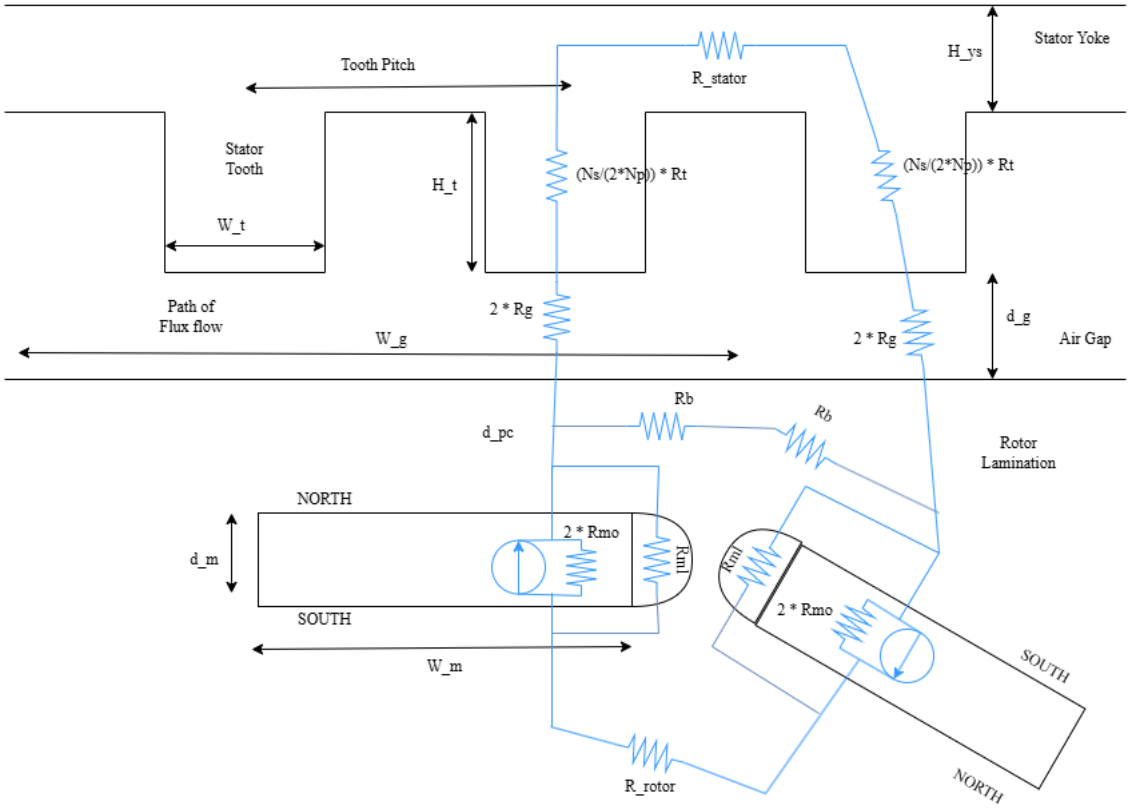

Figure 3.8: Representation of Flow of Flux Lines in the Open Magnetic Circuit

Since the rotor core has high permeability in the path of flux flow (pole cap region) and does not saturate, allowing the flux flow at no load condition, the reluctance was assumed low compared to the air gap and magnet and can hence, be neglected. Figure 3.9 illustrates the equivalent circuit after this simplification.

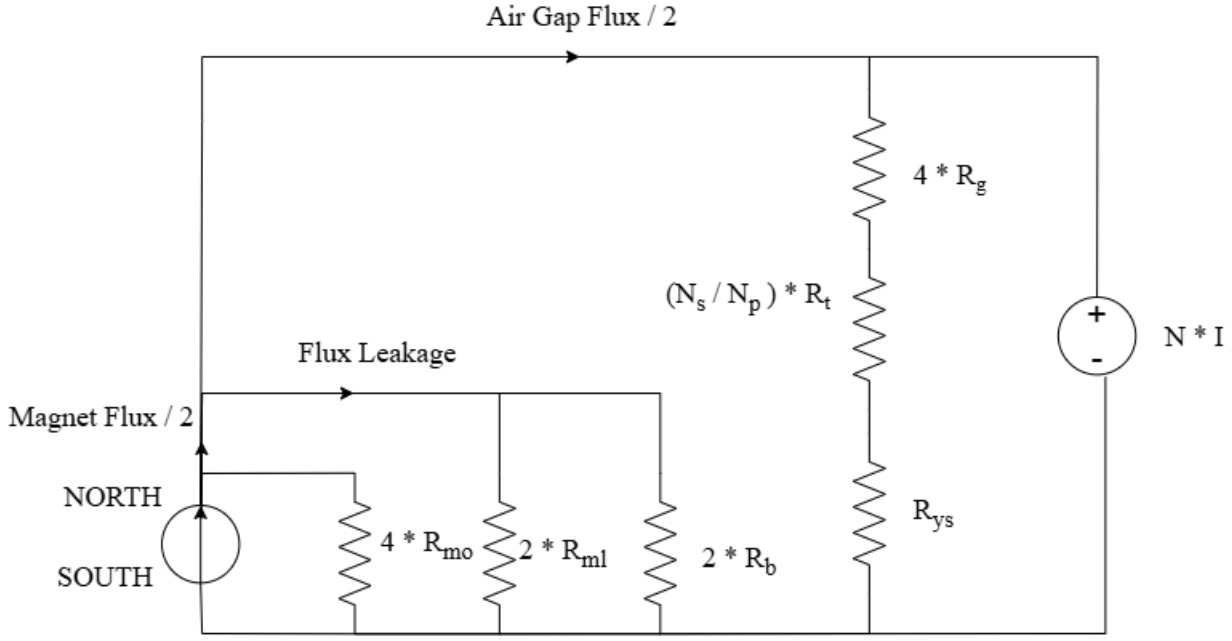

Figure 3.9: Representation of Magnetic Equivalent Circuit

A MEC was applied to investigate the saturation at the critical points such as the stator tooth and bridge of the rotor. It also helped in modeling the flux density at the air gap, which gave the flux linkage and magnetic loading needed to calculate the electromagnetic torque [54]. This modeling approach is analogous to the electrical systems described in Table 2.2.

The path of flux leakage consists of the reluctance of the bridge and the magnet air barrier between consecutive poles. Considering the closed loop to be in parallel, the effective reluctance (in H^{-1}) was calculated using Equation 3.51 [43], [44], [54].

$$R_m = \frac{4 * R_{mo}}{1 + 2 * \eta + 2 * \beta} \tag{3.51}$$

where η and β are flux ratios $\frac{R_{mo}}{R_{ml}}$ and $\frac{R_{mo}}{R_b}$ respectively [54].

The air gap, rotor, stator tooth, and stator yoke are in series; hence, their effective reluctance were estimated by summing the individual reluctance. This is shown in Equation 3.52 [43], [44], [54].

$$R_{tot} = R_m + 4 * R_g + \frac{N_t}{N_p} * R_t + R_{ys} \tag{3.52}$$

The internal reluctance of the magnet was calculated using Equation 3.53.

$$R_{mo} = \frac{d_m}{\mu_m * \mu_0 * W_m * L_{stack}} \tag{3.53}$$

The flux leakage must take into account the reluctances of the air barrier and bridge section, which was calculated using Equations 3.54 and 3.55, respectively.

$$R_{ml} = \frac{d_m}{\mu_0 * (\frac{d_m}{2} + \frac{(1-K)}{2} * W_m) * L_{stack}} \tag{3.54}$$

$$R_b = \frac{\frac{d_m}{2} + \frac{(1-K)}{2} * W_m}{\mu_{rotor} * \mu_0 * d_{bridge} * L_{stack}} \tag{3.55}$$

The reluctance of the air gap between the rotor and stator was estimated by using Equation 3.56.

$$R_g = \frac{d_{eg}}{\mu_0 * W_g * L_{stack}} \tag{3.56}$$

where d_{eg} is the effective air gap thickness (in m) with the implementation of the Carter Coefficient.

The reluctance of the tooth was calculated using Equation 3.57.

$$R_t = \frac{H_{slot}}{\mu_0 * \mu_{stator} * W_t * L_{stack}} \tag{3.57}$$

The reluctance of the stator yoke was calculated using Equation 3.58.

$$R_{ys} = \frac{\frac{N_t}{N_p} * \tau_s}{\mu_0 * \mu_{stator} * H_{ys} * L_{stack}} \tag{3.58}$$

3.7.1 Flux Density Distribution in Air Gap

The flux density in the air gap was investigated by solving the flow in the equivalent circuit as shown in Figure 3.9. The flux density in the air gap was estimated by the remanent flux density derived from the BH curve, using the flux division method [54].

$$\phi_g = \frac{4 * R_g + R_m + \frac{N_t}{N_p} * R_t + R_{ys}}{4 * R_g} * \phi_r \implies B_g = \frac{4 * R_g + R_m + \frac{N_t}{N_p} * R_t + R_{ys}}{4 * R_g} * B_r * C_\phi \tag{3.59}$$

B_g defines the magnet's contribution to the flux density at the air gap.

The flux produced by the coil was considered by the following Equation 3.60 [13].

$$\phi_{coil} = \frac{N_{ph} * I_{phase}}{R_{tot}} \tag{3.60}$$

Therefore, the total flux in the air gap is the summation of the individual components which was calculated using Equation 3.61.

$$\phi_{tot} = \phi_g + \phi_{coil} \implies B_{tot} = \frac{\phi_{tot}}{A_g} \tag{3.61}$$

3.7.2 Investigation of Saturation Point at the Bridge

The magnetic flux is saturated on the rotor yoke at the bridge to avoid flux leakage and prevent cross-magnetization. This minimizes the cogging torque and allows the flux to pass through the air gap, increasing the machine's efficiency [19]. The rotor material saturates when the flux density in the rotor exceeds 1.2 T ($B_{rot} \geq 1.2T$) [25].

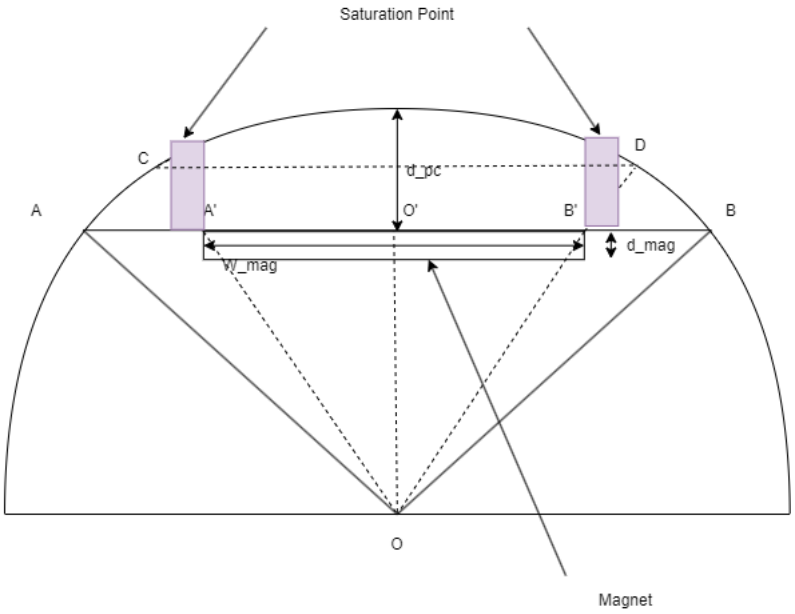

Figure 3.10: Representation of Saturation Point on Magnetic Air-Barrier on the Rotor

Applying KCL to the point where the magnet and the air gap join in Figure 3.9 the leakage flux was calculated using Equation 3.62 [54].

$$\phi_{leakage} = \frac{\phi_{mag}}{2} - \frac{\phi_g}{2} \tag{3.62}$$

where the ϕ_{mag} (in Wb) was calculated using the OP from the BH curve.

The bridge flux density was calculated from the leakage flux, as seen in Equation 3.63.

$$B_{bridge} = \frac{\phi_{leakage}}{d_{bridge} * L_{stack}} \tag{3.63}$$

The magnet's position can be adjusted by varying the coefficient K_{dpc}. This coefficient was chosen such that $B_{bridge} \geq 1.2T$, and the flux in the air gap meet the torque demands of the machine.

3.7.3 Flux Linkage Estimation

The flux linkage is caused by two components - mutual linkage which is due to the flux of the magnet linking with the coil through the slots and self linkage which occurs in loaded condition.

The mutual linkage was calculated by Equation 3.64.

$$\lambda_{mutual} = N_{\frac{turns}{pole}} * \phi_g \tag{3.64}$$

where ϕ_g is the flux in the air gap due to the magnet.

The self-linkage is evaluated under load conditions because the coil in the stator acts as a solenoid, generating a magnetic field around it that links with itself [13], [31]. This was calculated using Equation 3.65 [13], [31].

$$\lambda_{self} = N_{\frac{turns}{pole}} * \phi_{coil} \tag{3.65}$$

The total flux linkage was calculated by summing up the two components using Equation 3.66 [13], [31].

$$\lambda_{total} = \lambda_{self} + \lambda_{mutual} \implies N_{\frac{turns}{phase}} * (\phi_g + \phi_{coil}) \tag{3.66}$$

3.7.4 Back-EMF

According to Faraday's law, an EMF is induced due to a change in flux in the conductors. This is shown in Equation 3.67 [24], [55].

$$E_b = -\sum_{j=1}^{N_{turns}} \frac{d\phi_j}{dt} \tag{3.67}$$

where j is the number of active conductors. The flux change when the rotor rotates induces EMF, thus, Equation 3.68.

$$E_b = -\sum_{j=1}^{N_{turns}} \frac{d\phi_j}{d\theta} * \frac{d\theta}{dt} \tag{3.68}$$

where $\frac{d\theta}{dt} = \omega_r$ is the angular velocity (in $\frac{rad}{s}$).

Equation 3.68 implies the back-EMF is calculated using Equation 3.69.

$$E_b = K_e * \omega_r \tag{3.69}$$

where $K_e = 2 * N_{tc} * \phi_g$ is the motor constant (in $\frac{V-s}{rad}$).

3.7.5 Electromagnetic Torque and Electromagnetic Power Estimation

Electric loading is defined as the amount of current supplied to the motor's stator winding relative to its size, typically expressed as ampere-turns per unit length of the stator core or air gap circumference. It is a function of phase current, stator inner diameter, and turns per phase. Based on the stator dimensions and winding selected, the electric loading was evaluated using Equation 3.70 [12], [13].

$$A_{load} = \frac{2 * Phases * N_{ph} * I_{phase}}{\pi * D_{inStat}} \tag{3.70}$$

The torque per rotor volume depends on the magnetic loading [52] and the electric loading [12]. The torque per rotor volume was calculated using Equation 3.71

$$TRV = \sqrt{2} * A_{load} * B_g * \cos\phi \tag{3.71}$$

The electromagnetic torque was calculated by the torque per rotor volume and the volume of the rotor [12] using Equation 3.72.

$$T_{em} = TRV * V_{rotor} \tag{3.72}$$

Electromagnetic power depends on the rotor speed and the electromagnetic torque and was calculated using Equation 3.73.

$$P_{em} = T_{em} * \omega_{base} \tag{3.73}$$

3.8 Magnet Dimension Optimization

Figure 3.11 is a flowchart describing steps to optimize the magnet dimensions. This can be done by altering the coefficient values K_m and K_{dm}. The coefficient K_m alters the width of the magnet, and K_{dm} alters the thickness of the magnet.

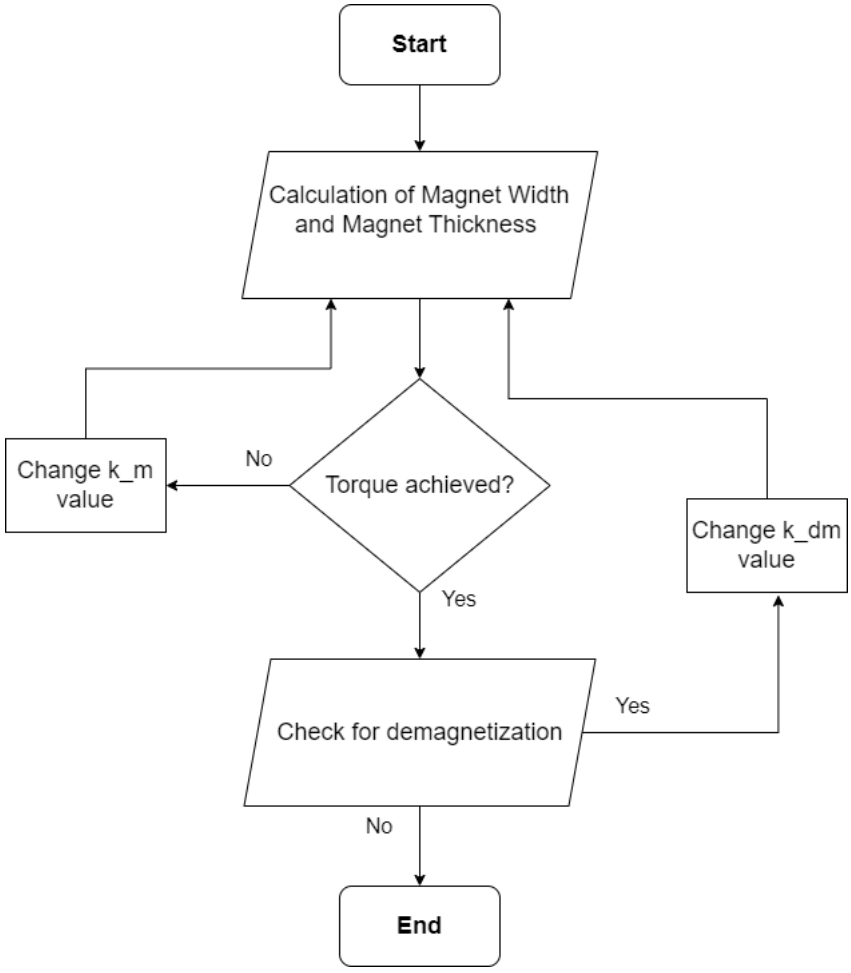

Figure 3.11: Flowchart to Optimize the Magnet Dimensions Based on Coefficient Method

The following steps were taken to optimize the dimensions.

1 The preliminary dimensions were calculated based on the analytical equations established.

2 The dimensions were used to calculate the flux densities at different parts of the machine using MEC and further calculate the electromagnetic torque.

3 The magnet width was altered iteratively by changing the value of k_m. This step was continued till the torque and flux densities were achieved to the set values in the input.

4 After this step is completed, the thickness of the magnet was investigated for ID. The value of k_{dm} was altered until the magnet does not undergo ID at full load current.

3.9 Electrical Machine Sizing Computational Tool

This tool was divided into five Python script files. They contained functions with analytical equations derived between the motor performance and sizing parameters. Figure 3.12 describes the schematic representation of data flow.

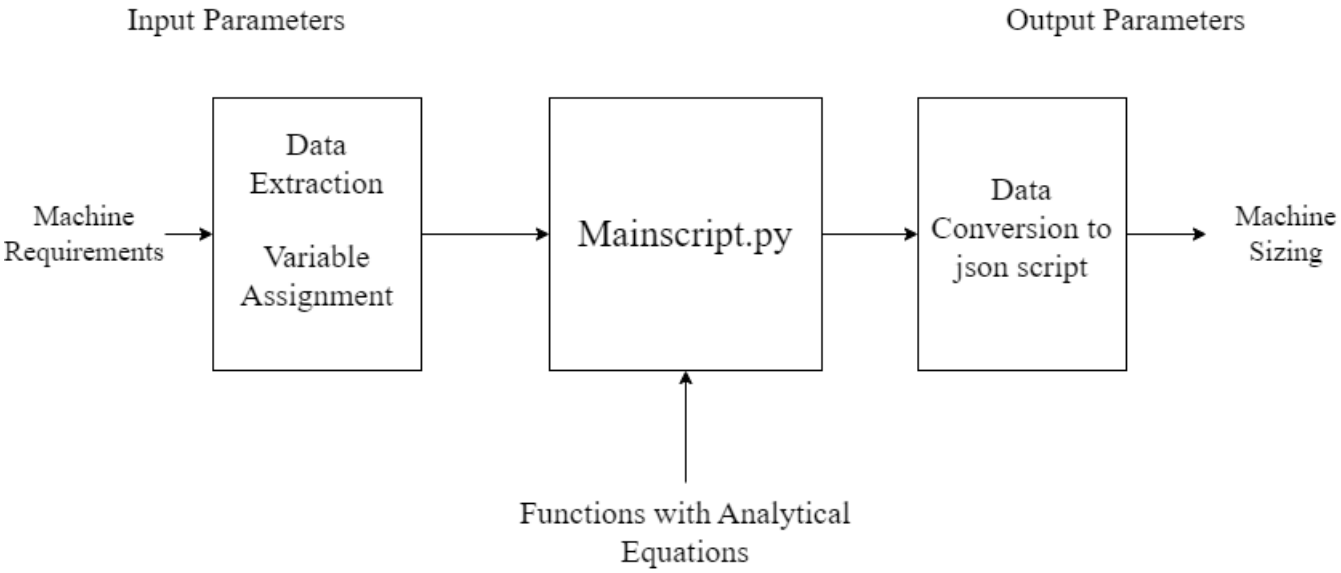

Figure 3.12: Schematic Representation Describing the Flow of Data in Different Script Files

The machine requirements (Fixed variables) and pre-defined values (adjustable and material constants), which are the input to the tool, were placed in the json script as a dictionary with variable keys. These values were accessed using the data extraction script, and variables were assigned in the data setup script that could be used by the Python scripts.

The tool had four Python scripts containing functions that used analytical equations established for machine design. Each script focused on an individual component of the machine design (dependent variables). The base parameter script file evaluated the machine's overall sizing. Similarly, the stator and rotor parametrizations were done in the stator dimensioning and rotor dimensioning script files, respectively. The PM modeling, MEC, electromagnetic torque, power, and losses were solved using the electromagnetic performance script file functions.

The main script ran the computational tool through individual function calls. The machine requirements were accessed and given as inputs to the individual function calls, solving the analytical equations. This was then converted to json format to view the values of the machine design and electromagnetic calculations.

4
Results

The computational tool was developed using the Python platform for AVL MTC Motortestcenter AB. Its focus was to establish analytical relationships between performance parameters and machine sizing parameters that help in the design parameterization of IPMSM. This computational tool enables a quick method of making design choices.

This section focuses on tool validation by comparing it with the FEM software output such as MotorCAD. The sizing parameters calculated in the tool were fed as input in the MotorCAD, and the 2-D model was assessed for two different machine requirements. The electromagnetic calculations were validated. The results are detailed in the order based on the objectives set.

4.1 Overall Machine Sizing

First, the overall machine sizing parameters were established. This laid the foundation for the different components of the IPMSM.

4.1.1 Rotor Dimensions

The required rotor volume was assessed for the required torque. The spacing and cooling method choice determines the TRV, which further constrains the rotor volume.

As mentioned in Section 3.3.1, the rotor dimensions were calculated. The rotor dimensions (D_{rotor} and L_{stk}) were assessed by comparing Equations 3.1, 3.2, and 3.3.

$$D_{rotor} = \sqrt[3]{\frac{4 * RatedTorque * p}{TRV * AspectRatio * \pi^2}} \tag{4.1}$$

The diameter played a key role in the space available to place the magnet and also defined the torque that could be generated for the specific application.

$$L_{Stk} = \frac{\pi * D_{rotor}}{p} * AspectRatio \tag{4.2}$$

The stack length was critical for the area involved in flux transfer between the rotor and stator. Hence, it affected the amount of force that could be generated.

4.1.2 Stator Dimensions

The stator's outer diameter was estimated after fixing the rotor's diameter and selecting a split ratio based on the rotor's position. The stator's outer diameter played a vital role

in bringing continuity to the flux flow circuit.

$$D_{OuterStator} = \frac{D_{rotor}}{SplitRatio} \tag{4.3}$$

The stator's inner diameter was calculated by selecting the air gap thickness required to achieve the machine's performance. The designer can make the air gap thickness selection based on the performance requirement and rotor configuration [3], [31].

$$D_{InnerStator} = D_{rotor} + 2 * d_g \tag{4.4}$$

The inner diameter played a significant role in the winding, slot, and tooth geometry and size design choices, thus affecting the electric loading for the required performance.

4.2 Stator Profile Sizing

4.2.1 Winding Selection

The winding design selected for the thesis study was a distributed, full pitch, and single-layer winding. The key parameters necessary while defining a winding design for an EM were turns per phase, coils per phase, and turns per coil. The relations used to derive these parameters are given by Equation 4.5, Equation 4.6, Equation 4.7 respectively.

$$T_{ph} = \frac{EMF * \sqrt{2}}{\pi * K_w * \phi_g * f} \tag{4.5}$$

$$N_{cp} = \frac{N_{ss}}{m * N_p} \tag{4.6}$$

$$N_{tc} = \frac{n * T_{ph}}{N_{cp} * N_p} \tag{4.7}$$

4.2.2 Tooth and Slot Dimensions

The stator tooth serves as a path for the flux to flow. The width of the tooth was estimated using the material saturation flux density as given by Equation 4.8.

$$W_{tht} = \frac{N_p * B_{gPeak} * W_g}{N_{ss} * B_{tpk}} \tag{4.8}$$

The slot's size should accommodate all the conductors; that is, its area should be greater than the area occupied by winding conductors. Equation 4.9 gives the estimate of the slot's area.

$$A_s = \frac{N_{tc} * A_c}{K_f} \tag{4.9}$$

Using the geometric equations, the slot width was estimated using the tooth width and tooth pitch by Equation 4.10.

$$W_{sb} = \tau_s - W_{thb} \tag{4.10}$$

The slot and tooth depth were estimated using Equation 4.11 by the area and width of the slot.

$$H_s = \frac{A_s}{1.1 * W_{sb}} \tag{4.11}$$

4.2.3 Carter Coefficient and Effective Air Gap Thickness

The fringing effect of field lines was estimated using a constant known as Carter Coefficient and estimated by Equation 4.12.

$$K_c = \frac{K_{th} * (4.44 * d_g + 0.5 * W_{sb})}{K_{th} * (4.44 * d_g + 0.5 * W_{sb}) - W_{sb}^2} \tag{4.12}$$

The effective thickness of the air gap was estimated using the Carter Coefficient and given by Equation 4.13.

$$d_{eg} = K_c * d_g \tag{4.13}$$

4.3 Rotor Profile Sizing

Once the overall machine and the stator components are sized, the magnet volume and geometry determine the magnetic loading [12], [13]. This parameter is necessary to understand the torque, power, and efficiency of the machine.

4.3.1 Magnet Width

The magnet width was assessed based on the geometrical constraints of the rotor core and trigonometric principles. The maximum possible magnet width for a choice of α was established, as shown in Equation 4.14.

$$W_{mag} = \alpha_p * D_{rotor} * \sin\frac{\theta_p}{2} \tag{4.14}$$

However, a coefficient K_m was introduced, which helped to resize the width of the magnet. Thus, the algorithm is flexible enough to alter the magnet volume to balance the cost and performance of the EM.

This was investigated by following the steps mentioned in Section 3.8 and the new magnet width was calculated using Equation 4.15.

$$W'_{mag} = K_m * W_{mag} \tag{4.15}$$

4.3.2 Magnet Thickness

The thickness of the magnet is an essential parameter in investigating its ability to perform in the flux-weakening point for high-performance machines [30]. This dictates the magnet's ability to handle the demagnetizing field acting on it [30].

Based on the open-circuit flux transfer condition, the magnetomotive force across different components in this circuit gives the thickness of the magnet and was established by Equation 4.16.

$$d_{mag} = (-(\frac{B_{rot}}{\mu_0 * \mu_{rot}} * d_{pc} + \frac{B_g}{\mu_0} * d_g + \frac{B_t}{\mu_0 * \mu_s} * d_t + \frac{B_{ys}}{\mu_0 * \mu_s} * d_{ys})) * \frac{\mu_0 * \mu_m}{B_{mag} - B_r} \quad (4.16)$$

Further, a coefficient K_{dm} was introduced and iteratively investigated. This helped in resizing the thickness of the magnet by following the steps mentioned in Section 3.8 and applying Equation 4.17.

$$d'_{mag} = K_{dm} * d_{mag} \quad (4.17)$$

4.3.3 Magnet Distance from Pole-Cap and Bridge Thickness

After sizing the magnet finding an optimum position to perform efficiently is very important. The magnet needs to be at a reasonable distance from the pole cap, which would allow sufficient flux transfer across the air gap. It also needs to have rotor lamination that protects the magnet from unnecessary damage [30].

Equation 4.18 was established to calculate the pole cap thickness based on geometrical constraints and trigonometric ratios.

$$d_{pc} = \frac{D_{rotor}}{2} - \frac{W_{mag}}{2 * \tan(\frac{\theta_m}{2})} \quad (4.18)$$

Using similar triangle principles, the bridge thickness was related to the pole cap thickness, as shown in Equation 4.19. Generally, a 2 mm bridge thickness is considered, which prevents active participation in flux transfer due to saturation. It is also thick enough to handle the stresses acting on it [25].

$$d_{bridge} = \frac{\tau_p - \tau_m}{\tau_p} * d_{pc} \quad (4.19)$$

However, the tool allows us to reevaluate the pole cap thickness using the coefficient method. This can move the magnet closer or further into the rotor core. The designer has the choice based on the design criteria, as shown in Equation 4.20.

$$d'_{pc} = K_{pc} * d_{pc} \quad (4.20)$$

4.4 Comparisons of Python Algorithm with Two Different Machines

Two case studies of different machine requirements were conducted, and the validation was made by comparing the results with the outcome of the MotorCAD simulation.

The comparisons were made with templates available in MotorCAD (case study 1) and paper titled " Design and Development of High Torque, Compact and Energy Saver PMSM Motor for Hydraulic Applications" (case study 2) [56].

4.4.1 Case Study 1

Table 4.1 presents the motor requirements of a template from the MotorCAD software. This template's rated torque and power are 158 Nm and 100 kW, respectively. It was a high-speed machine rated at 6000 rpm. For a voltage of 400 V at the DC-link, the RMS current at a full load condition required for the power is 221 A.

Table 4.1: Machine Requirement From MotorCAD Template

Torque [Nm]	158
Power [kW]	100
DC Bus Voltage [V]	400
Fundamental Frequency [Hz]	400

The overall machine sizing for the given requirements was calculated in the Python tool, and these values are compared and tabulated in Table 4.2. The TRV selected for this motor was 66446 $\frac{Nm}{m^3}$ with a choice of aspect ratio and a split ratio of 1.4635 and 0.696, respectively.

The overall dimension anomaly was a 1 mm difference between the template and Python tool in the rotor outer diameter and stator inner diameter.

Table 4.2: Comparison of Overall Machine Sizing

Parameter	MotorCAD template	Python model
Stator Outer Diameter [mm]	250	250
Stator Inner Diameter [mm]	175	174
Rotor Outer Diameter [mm]	174	173
Stack Length [mm]	100	100

After the machine was sized, the individual components of the rotor and stator were calculated based on the analytical expressions derived. This comparison was drawn in Table 4.3. The template and the developed tool account for 48 slots and an 8-pole machine. The magnet's width matches, but the magnet's thickness shows a large variation. A marginal difference was seen in the slot and tooth dimensions.

Table 4.3: Comparison of Rotor and Stator Profile Sizing

Rotor Profile Sizing		
Parameter	MotorCAD	Python
Number of poles	8	8
Magnet width [mm]	45	45
Magnet thickness [mm]	4	11
Stator profile sizing		
Number of slots	48	48
Tooth width [mm]	6.865	7.113
Slot width [mm]	4.453	4.2098

Electromagnetic calculations were made to evaluate the machine's performance based on the sized components, and the comparison was tabulated in Table 4.4. The parameters compared were the flux densities, both average and peak, at critical points such as the air gap and tooth tip. Additionally, the output performance (torque and power) was also investigated.

Table 4.4: Comparison of Electromagnetic Calculations

Parameter	MotorCAD	Python
Air gap flux density (average) [T]	0.506	0.34758
Air gap flux density (peak) [T]	1.389	0.54598
Stator tooth flux density (peak) [T]	1.563	0.757437
Output Torque [Nm]	161	127.5
Output Power [W]	100000	80720

As sizing affects machine performance, the differences seen in Table 4.4 were the consequences of the differences in sizing.

4.4.2 Case Study 2

Another case study was made on an IPMSM used for hydraulic applications, and the design strategy was detailed in a journal titled "Design and Development of High Torque, Compact and Energy Saver PMSM Motor for Hydraulic Applications" [56]. This was a low-speed (1000 rpm) and low-power application. The motor requirements are given in the Table 4.5 [56]. For this low-power application, the required full load current accounted for 72 A for a similar DC-link voltage of 440 V.

Table 4.5: Machine Requirements Case 2

Torque [Nm]	333.01
Power [W]	35800
DC Bus Voltage [V]	440
Fundamental frequency [Hz]	66.67

The TRV, aspect ratio, and split ratio were computed for the algorithm from the rotor and stator dimensions of the journal model. Thus, the tool resulted in dimensions as shown in Table 4.6. Based on this, the rotor and stator profiles were calculated and used for electromagnetic comparisons.

Table 4.6: Overall Machine Sizing Comparisons

Overall Machine Sizing		
Parameters	Journal	Python
Rotor Outer Diameter [mm]	269	269
Stack Length [mm]	90	90
Stator Outer Diameter [mm]	400	400
Stator Inner Diameter [mm]	270	270

As seen in Table 4.7, the magnet's sizing after optimization was accurate. However, the tooth dimensions estimated in the tool are two times the size in the journal model. Further, the slot dimensions for the model were not available.

Table 4.7: Rotor and Stator Profile Sizing Comparisons

Rotor Profile Sizing		
Parameters	Journal	Python
Number of poles	8	8
Magnet width [mm]	70	70
Maximum magnet thickness [mm]	18	18
Stator Profile Sizing		
Number of slots	48	48
Tooth width [mm] (top)	6.59375	12.849
Tooth width [mm] (bottom)	5.83885	12.738
Slot width [mm] (top)		5.92
Slot width [mm] (bottom)		4.933

A detailed flux density investigation was made at critical spots. The comparisons drawn included implementing the same sizing parameters in MotorCAD software. The different parts focused on were the air gap, tooth tip, stator yoke, and rotor bridge. Table 4.8 shows the comparisons made.

Table 4.8: Flux Density Comparisons at Critical Points

Parameter	Journal	Python	MotorCAD
Air gap flux density (average) [T]	0.633033	0.46735	0.7067
Stator tooth tip flux density (peak) [T]	2.04552	1.01842	1.18
Magnet flux density (average) [T]	0.775206	0.755769	
Bridge flux density [T]		1.285	2.167

The data to compare magnet flux density was not available in MotorCAD; similarly, the bridge flux density could not be validated compared to the values in the paper. The values of the flux densities show marginal differences with the outcome of the FEM solver being more accurate to the values observed in the journal.

Table 4.9 depicts the performance comparison of torque and power at the shaft.

Table 4.9: Output Performance Comparisons

Parameter	Journal	Python	MotorCAD
Output Torque [Nm]	333.01	322.874	336.32
Output Power [W]	35800	34711.376	363135

4.5 Sensitivity Analysis

The sensitivity analysis was made iteratively considering the model illustrated in case study 2 as the machine designed.

A variation in parameters such as air gap thickness, magnet width, pole arc to pole pitch ratio, and magnet strength is made, and their impact on the electromagnetic calculations was investigated. Further, the outcomes were compared with the FEM solver (MotorCAD) to validate the credibility of the tool.

This study followed a uniform color code throughout the analysis. The outcomes of the Python tool and MotorCAD were plotted in blue and orange respectively. The dotted lines represent their trendline.

4.5.1 Consequence of Variation in Air Gap Thickness

Table 4.10 provides the analysis of the electromagnetic calculations by varying the air gap thickness between 0.5 mm and 1 mm [11]. The tested parameters were the flux density in the air gap (average), flux leakage, output torque, and power.

Table 4.10: Comparison of Air Gap Thickness Variation

Parameter		Case 1	Case 2	Case 3
Air gap thickness (dg) [mm]		0.5	0.75	1
B_g (average) [T]	Python	0.47635	0.38974	0.342886
	MotorCAD	0.7067	0.6934	0.6817
Output Torque [Nm]	Python	322.874	287.7	253.208
	MotorCAD	336.32	324.21	314.5
Output Power [W]	Python	34711.3762	30930.202	27221.783
	MotorCAD	36135	34834	33791
Flux Leakage [Wb]		0.0002369	0.00077395	0.0010998

Figure 4.1 shows the trendlines of the air gap flux density (average) for the variation in air gap thickness. Though there was a large difference in the flux density values, both trendlines showed a decrease in the flux density with an increase in air gap thickness.

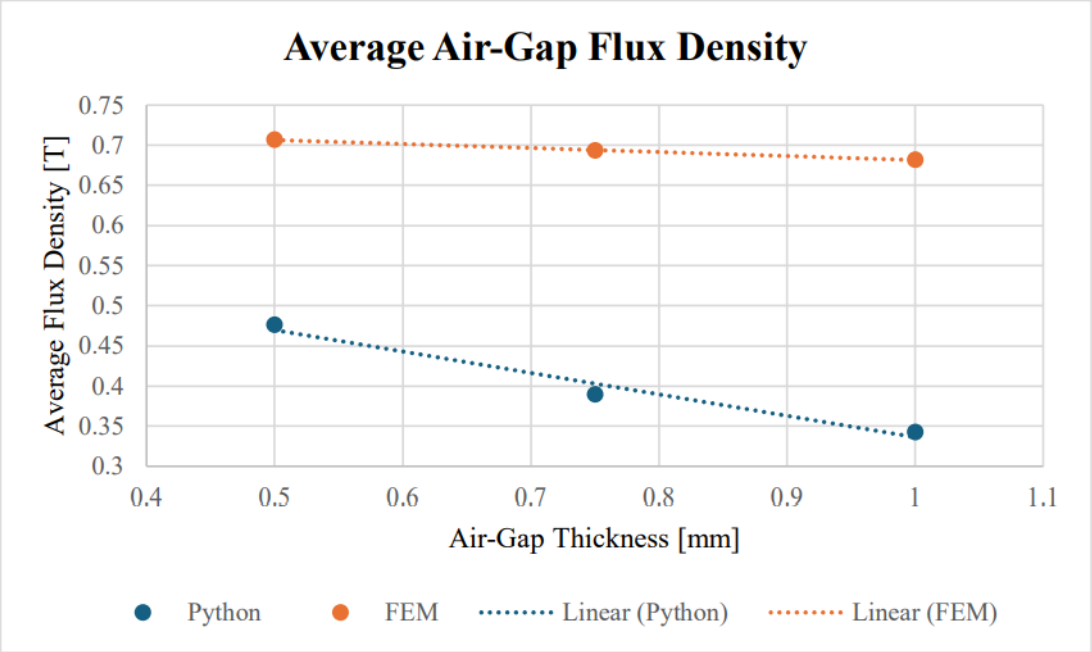

Figure 4.1: Consequence of Variation in Air Gap Thickness on Air Gap Flux Density

Figures 4.2 and 4.3 compare the influence of the Python tool and MotorCAD on output torque and output power, respectively, for variation in air gap thickness.

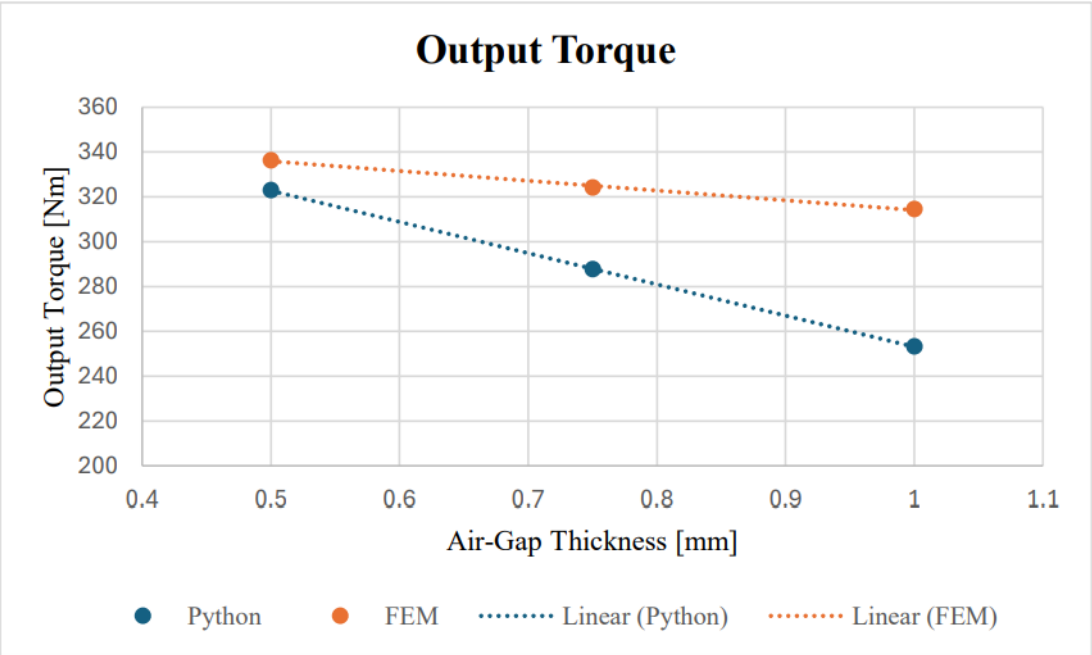

Figure 4.2: Consequence of Variation in Air Gap Thickness on Output Torque

They followed a similar pattern, that is, decreased performance for increased air gap thickness. The design choice of 0.5 mm thickness resulted in the desired performance.

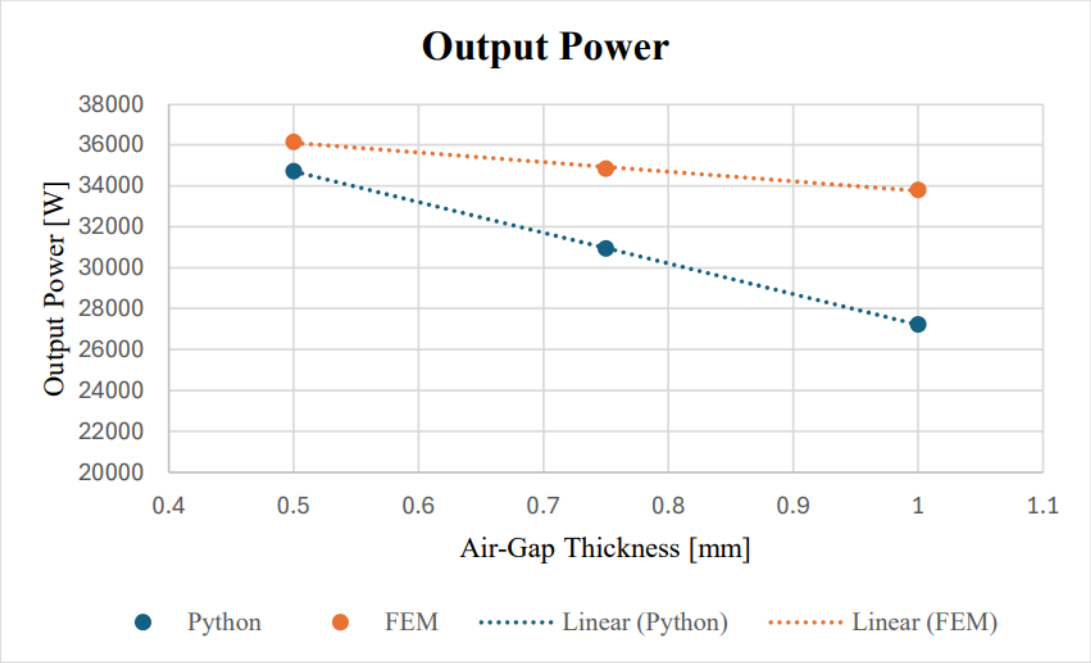

Figure 4.3: Consequence of Variation in Air Gap Thickness on Output Power

The flux leakage was calculated only in the Python computational tool and hence no comparison was drawn with the FEM solver (MotorCAD). Figure 4.4 shows the impact of air gap thickness variation on the flux leakage.

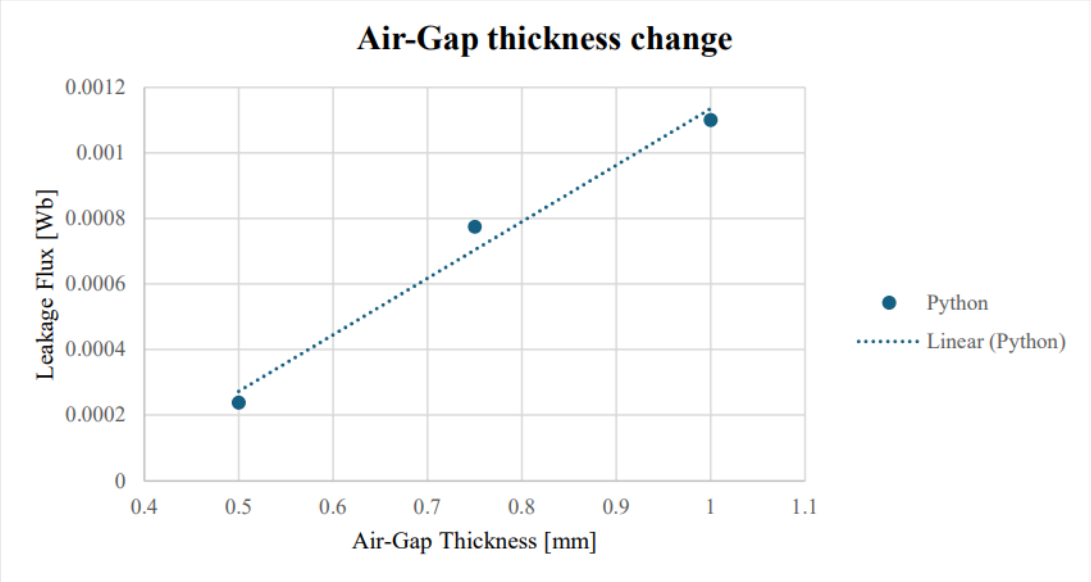

Figure 4.4: Consequence of Variation in Air Gap Thickness on Flux Leakage

It showed a considerable increase in the flux leakage with an increase in air gap thickness.

4.5.2 Consequence of Variation in Magnet Width

Since the air gap thickness of 0.5 mm replicates the model in the journal [56] and also was the value that gave the most efficient machine performance, the air gap thickness was

considered to be 0.5 mm for this analysis. Now, the magnet's width is iteratively varied between 60 mm and 75 mm, and the dynamics of the machine were validated.

Table 4.11 compares the Python tool and MotorCAD outputs for magnet width variation.

Table 4.11: Comparison of Magnet Width Variation

Parameter		Case 1	Case 2	Case 3	Case 4
Magnet Width (Wm) [mm]		60	65	70	75
B_g (average) [T]	Python	0.4278987	0.449612	0.467352	0.480504
	MotorCAD	0.5977	0.6521	0.7067	0.7612
Output Torque [Nm]	Python	306.786	306.786	322.873	336.953
	MotorCAD	305.33	322.02	336.32	348.56
Output Power [W]	Python	31068.783	32981.797	34711.376	36225.016
	MotorCAD	32805	34599	36135	37450

Figures 4.5, 4.6, and 4.7 illustrate the air gap flux density (average), output torque, and output power, respectively.

The trendlines of the Python tool and MotorCAD resulted in an increased air gap flux density with an increased magnet width.

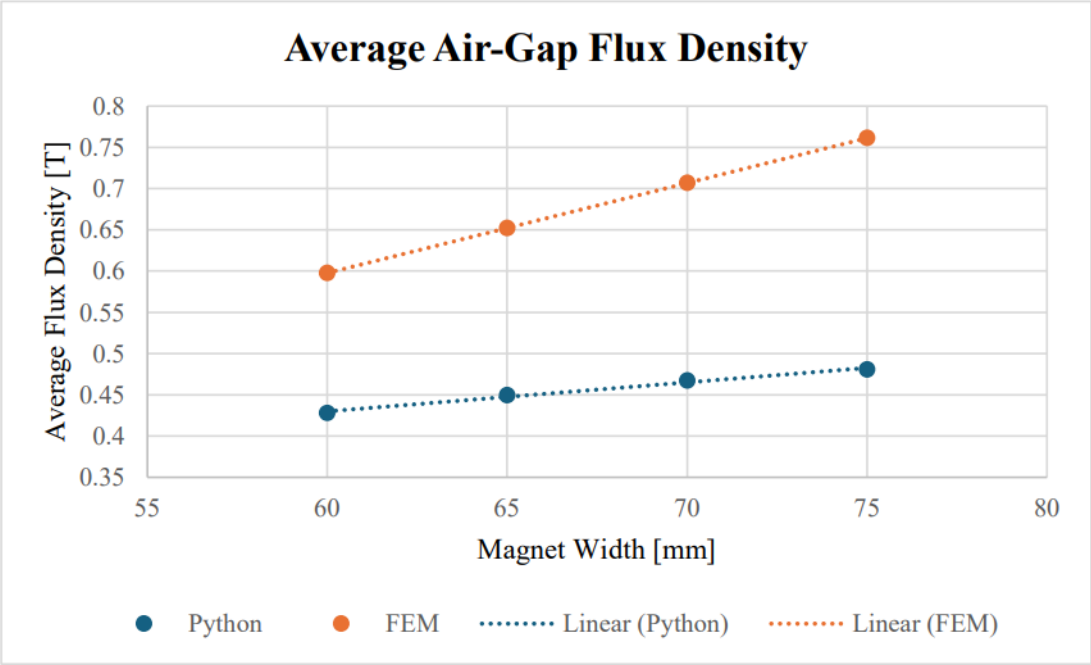

Figure 4.5: Consequence of Variation in Magnet Width on Air Gap Flux Density

Further, the torque and power showed a similar trendline, and the variations between the two models are comparable. It was observed that the torque and power increased equally with an increase in the magnet width.

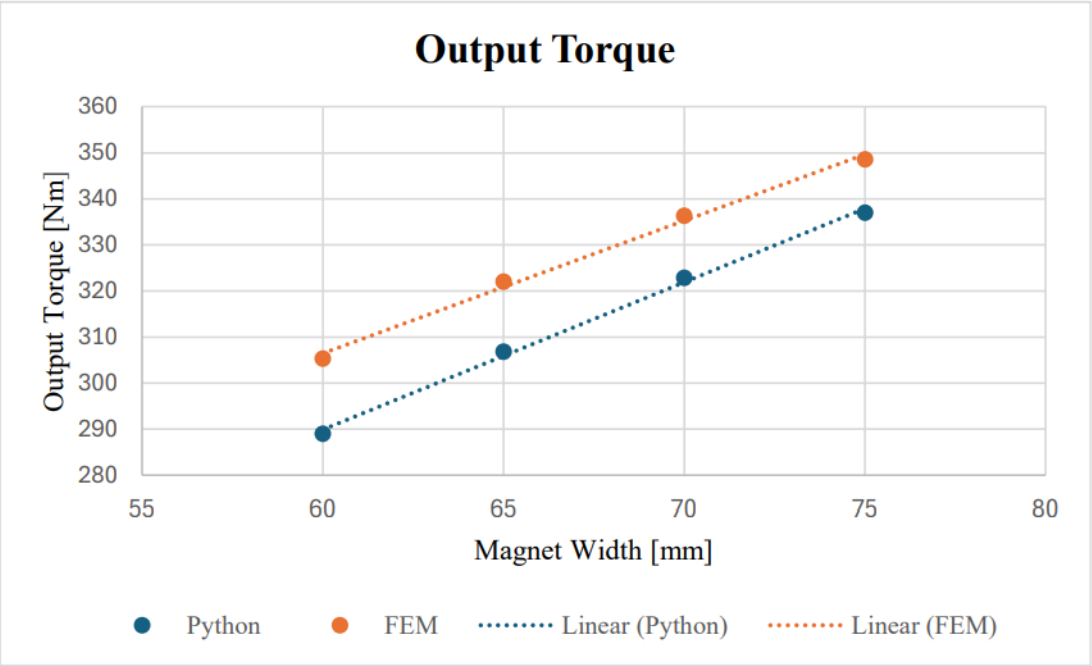

Figure 4.6: Consequence of Variation in Magnet Width on Output Torque

It was seen that a magnet width of 70 mm results in the least deviation among the two models.

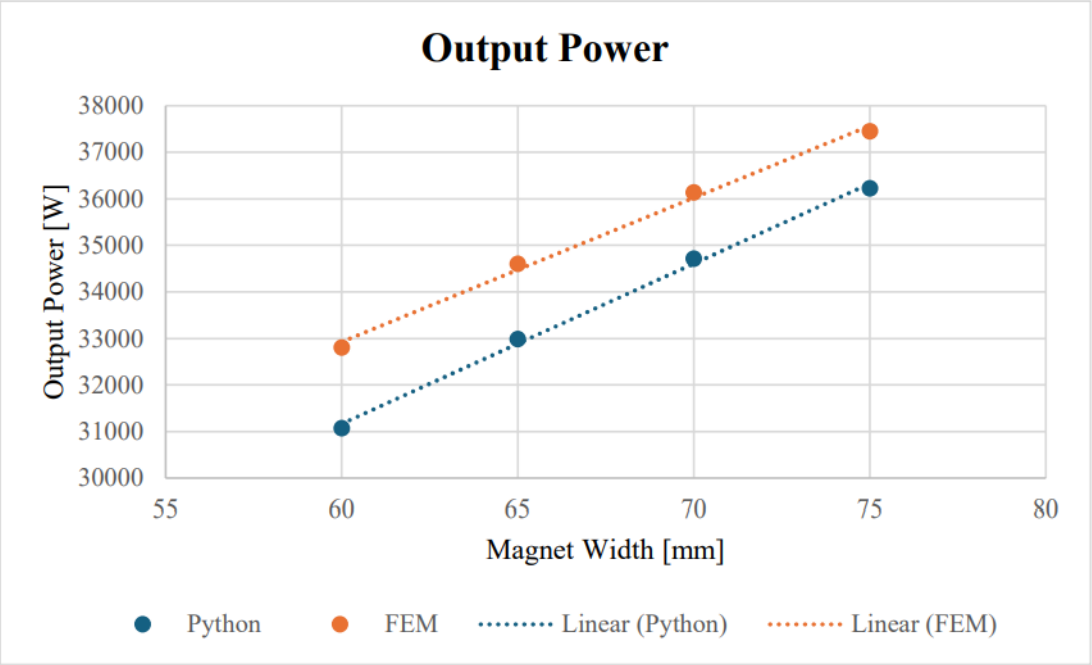

Figure 4.7: Consequence of Variation in Magnet Width on Output Power

4.5.3 Consequence of Variation in Pole-Arc to Pole-Pitch Ratio

In this analysis, the pole-arc (τ_m) to pole-pitch (τ_p) ratio was varied, and the machine's performance was assessed. Keeping the air gap thickness at 0.5 mm and maintaining the magnet width at 70 mm for all the cases, the simulation was run in MotorCAD and

Python Tool. The angle subtended by the magnet air barriers for individual variation in α was given as the embrace angle (electrical degrees). The embrace angle was used as input for analyzing the pole-arc to the pole-pitch ratio variations in MotorCAD.

The results of the simulation are logged in Table 4.12

Table 4.12: Comparison Made For α Variation

Parameter		Case 1	Case 2	Case 3	Case 4
α		0.7	0.75	0.8	0.85
Embrace Angle [Electrical degrees]		126	135	144	153
B_g (average) [T]	Python	0.424026	0.446597	0.46735	0.4440386
	MotorCAD	0.7019	0.7091	0.7067	0.7039
Output Torque [Nm]	Python	304.2735	313.964	322.874	312.863
	MotorCAD	340.64	338.05	336.32	333.95
Output Power [W]	Python	32711.688	33753.4836	34711.376	33635.108
	MotorCAD	36599	36321	36135	35880
Flux Leakage [Wb]		0.0005616	0.0003924	0.00023688	0.0004116

Figure 4.8 describes the variation in the average flux density in the air gap conducted for this analysis. The flux density decreased when α was varied from 0.8 to 0.85 for both models. On the other hand, the Python tool showed a decrease in the flux density with a decrease in α, while the MotorCAD simulation resulted in an increase between 0.8 and 0.75 and a decrease between 0.75 and 0.7.

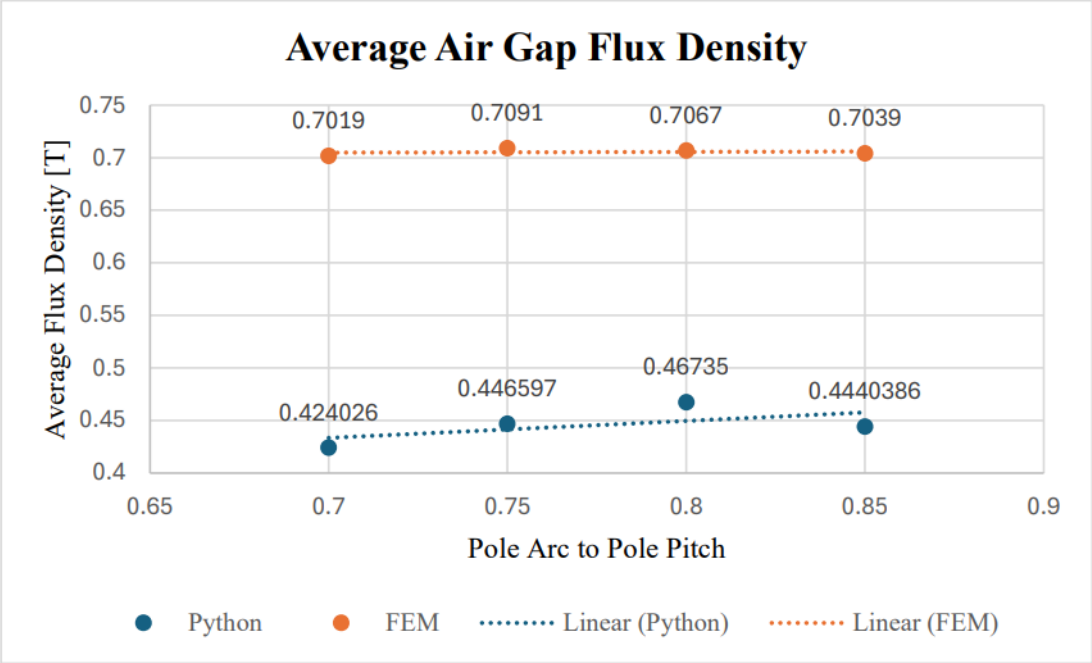

Figure 4.8: Consequence of Variation in α on Flux Density

Figure 4.9 and Figure 4.10 bring out the differences in the torque and power and their impact on a variation in α.

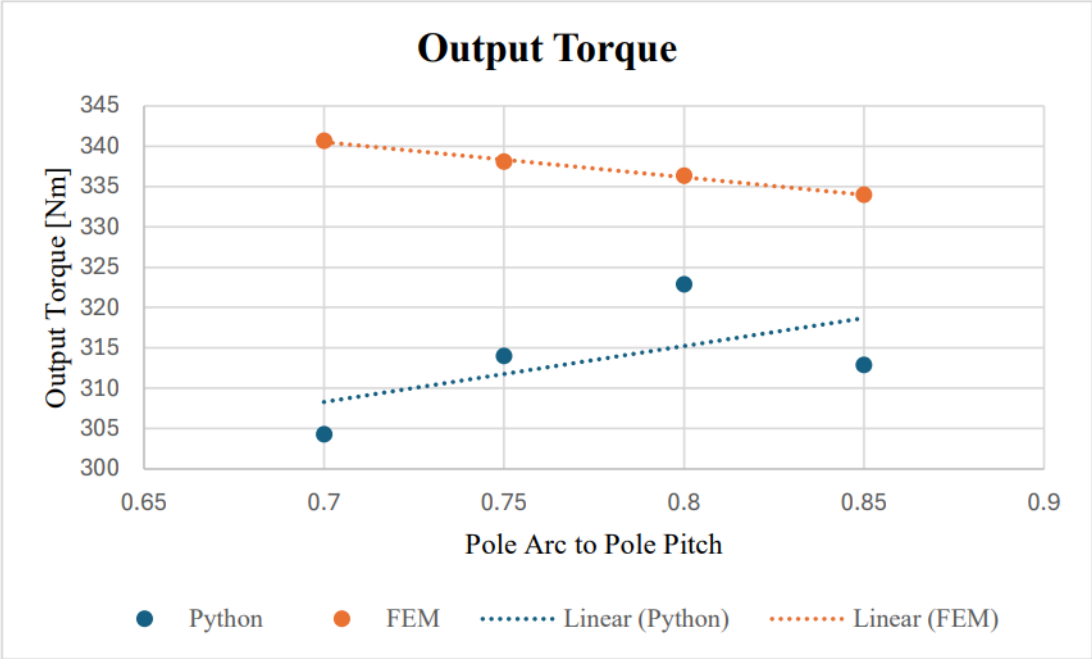

Figure 4.9: Consequence of Variation in α on Output Torque

The trendlines in torque and power followed opposite trends between the outcomes of the Python and MotorCAD. However, an α of 0.8 was a good design choice for an efficient machine and was reasonably close.

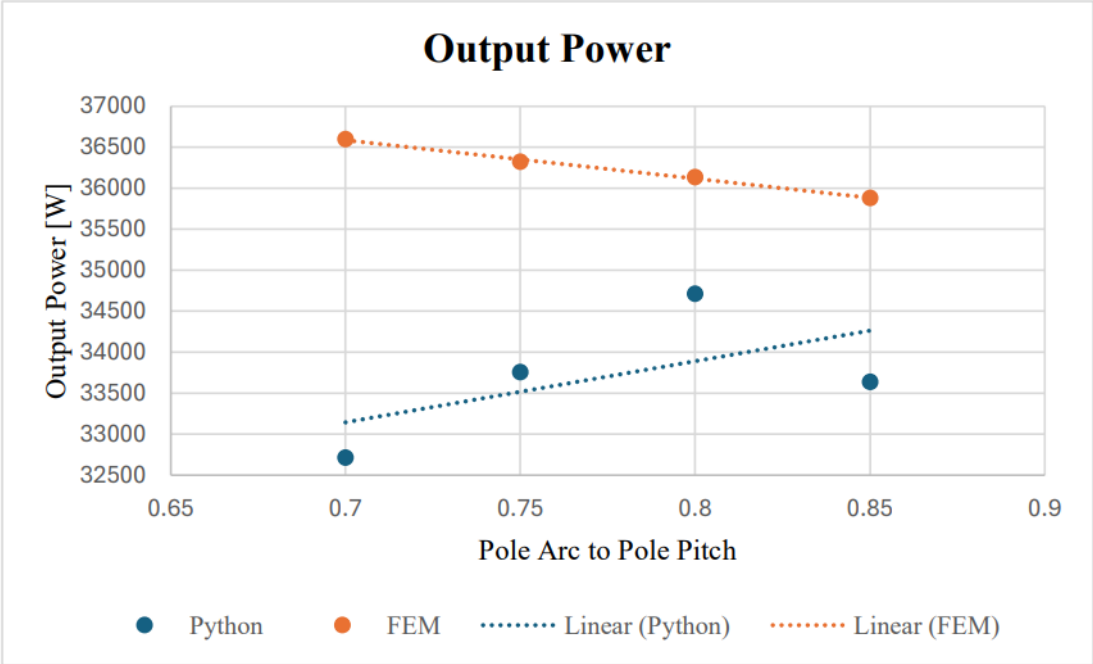

Figure 4.10: Consequence of Variation in α on Output Power

The plot in Figure 4.11 shows the variation in flux leakage. The leakage was the lowest when 0.8 was chosen for the design, resulting in efficient performance.

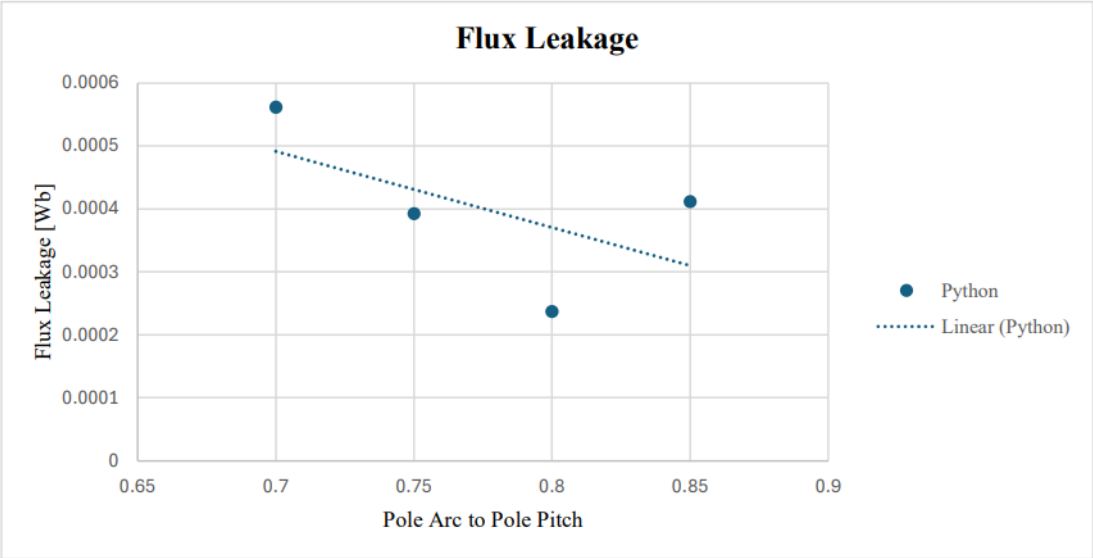

Figure 4.11: Consequence of Variation in α on Flux Leakage

4.5.4 Consequence of Variation in Magnet Grade

The effects of the change in magnet grade on the machine's performance were studied. Data from magnet grades N35 and N42 have remanence flux densities of 1.21 T and 1.31 T, respectively [32]. This analysis was conducted for the same magnet volume (100800 mm^3), and the air gap flux density, torque, and power were the studied parameters.

The Table 4.13 gives details on the studied parameter.

Table 4.13: Comparison Made For Variation in Magnet Strength

Parameter		Case 1	Case 2
Magnet Grade		N35	N42
B_g [T] (average)	Python	0.4673522	0.550467
	MotorCAD	0.7051	0.7681
Output Torque [Nm]	Python	322.874	358.56
	MotorCAD	336.7	361.81
Output Power [W]	Python	34711.376	38547.93
	MotorCAD	36176	38873

Figure 4.12 shows the air gap flux density variation with a change in magnet grade for the same magnet volume. Though the values showed deviation, the trend for both models remained similar. An increase in flux density with higher magnet strength was observed.

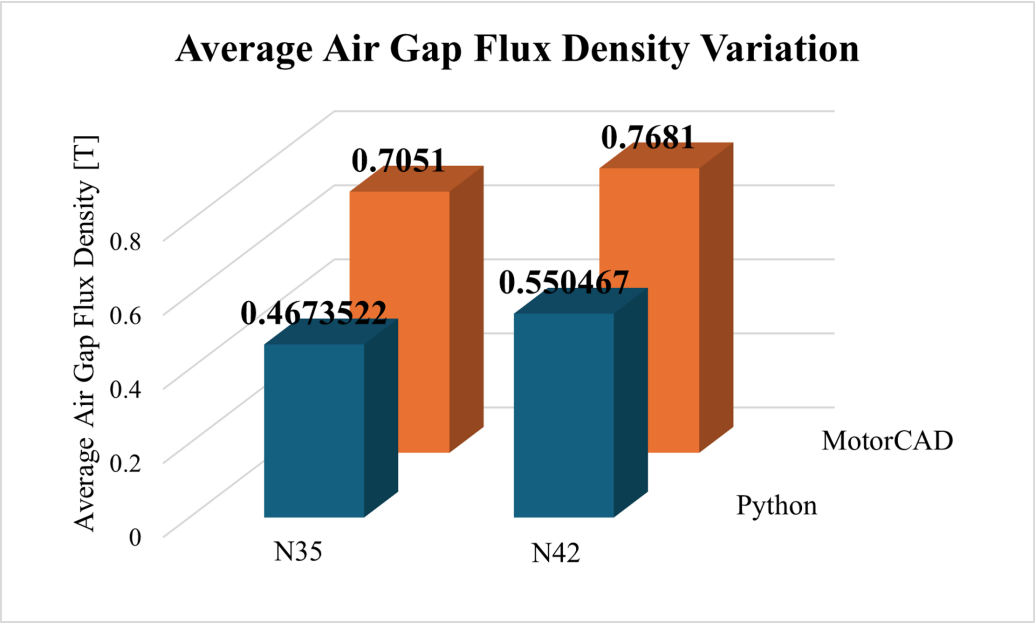

Figure 4.12: Consequence of Variation in Magnet Strength on Air Gap Flux Density

Figure 4.13 and Figure 4.14 illustrate the torque and power output, respectively, with higher magnet strength.

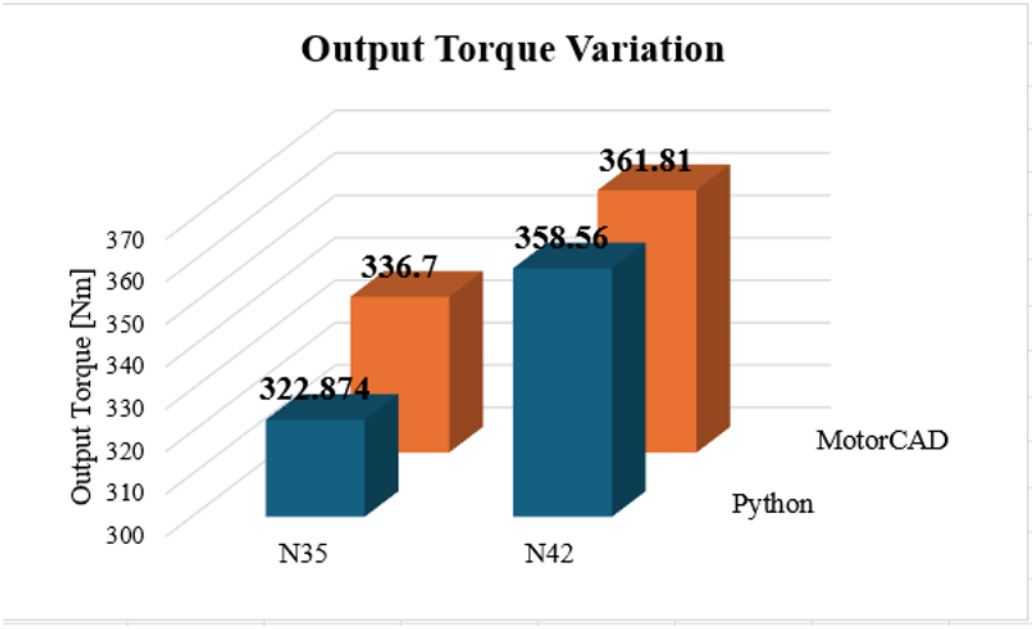

Figure 4.13: Consequence of Variation in Magnet Strength on Output Torque

They showed similar outcomes for torque and power. Higher magnet strength increased performance.

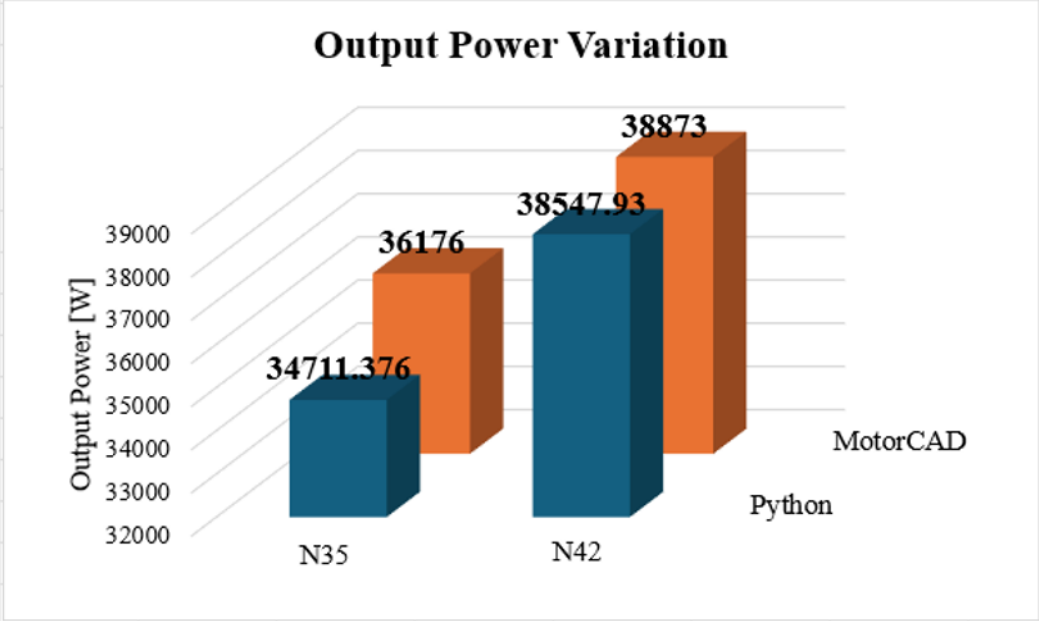

Figure 4.14: Consequence of Variation in Magnet Strength on Output Power

5
Discussion

The growing popularity of climate-neutral vehicles can be attributed to their low operating costs, evolving governmental regulations, and capability to operate with a zero-carbon footprint [2]. As EMs are key in these vehicles, there is a growing need for research on the design and sizing of these machines. The primary objective of this computational tool was to enable rapid prototyping and parametrization while reducing iteration time to explore several design combinations.

The main aim of this thesis was to develop a computational environment for designing IPMSM. This tool was developed using the Python platform. The algorithm estimated the machine's sizing parameters based on the machine's requirements using analytical equations. Two case studies were conducted using the tool for different machine designs.

Additionally, a sensitivity analysis was conducted to examine the dynamics, and the results were compared against those from a FEM solver for credibility. Analytical relations between sizing and performance parameters were established by considering geometric constraints and assumptions. The FEM solvers were able to reproduce similar output as machine requirements for the calculated design. Performance parameters (air gap flux density, torque, and power) were investigated by varying air gap thickness, magnet width, pole-arc to pole-pitch ratio, and magnet strength. While similar trends were observed between the two models for variations in air gap thickness, magnet width, and magnet strength, a contrasting trend emerged when varying the pole-arc to pole-pitch ratio.

5.1 Analytical Design of Machine Components

In machine design for automotive applications, the machine was initially sized to satisfy the vehicle's requirements. The analytical method provides reliable mathematical relations that are necessary for initial parameterization. An advantage of the analytical approach is its computational efficiency, enabling the rapid generation of numerous design combinations [57]. The selected design can be refined, based on application, material, and cost using computationally intensive methods such as FEA [57].

The computational tool focuses on providing the sizing of four key machine components: the rotor core, stator core, winding selection, and magnet. These components were designed using the machine's torque and power requirements. A generic and quick approach is followed for the sizing of machines (stator and rotor cores) based on torque requirements, TRV, aspect ratio, and split ratio [25], [26].

Assuming the back-EMF is sinusoidal, which offers smoother operation [12], distributed winding was selected. The choice of full pitch and single layer was made to streamline the winding design. A simple flat magnet with semi-circular air barriers was chosen to reduce the complexity of the design. The rotor core was assumed to have high permeability, reducing the number of unknown variables to calculate the initial thickness of the magnet.

The linear modeling approach was sufficient to model the magnet as the neodymium magnets show linear properties [16]. Further, only the second quadrant of the hysteresis curve was modeled because the design parameters of the magnet need to keep the operating point above the knee point, which occurs in the second quadrant [30]. The temperature-varying magnetic model was not implemented as it increased the complexity. So, it was assumed that the machine worked at a constant temperature.

5.2 Effect of Parameter Variation on Output

The computational tool was developed on the Python platform using the established analytical equations and MEC. The case study 1 was conducted to test the model's ability to size machines. This was accomplished by replicating a template available in MotorCAD, as discussed in Section 4.4.1. The overall machine size was comparable. However, it was observed that there were variations in the rotor outer diameter and stator inner diameter. This is because of the difference in the design approach between the two models. The MotorCAD (FEM solver) considers the sizing parameters as an input to the simulation environment, where the stator inner diameter is fixed based on the input, and the rotor outer diameter is calculated. On the other hand, the purpose of the tool developed was to estimate the sizing, which calculates the stator's inner diameter from the rotor structure.

Additionally, the dimensions of the slots and magnet in both models were similar. However, the magnet thickness showed a large difference, as seen in Table 4.3. This was mainly because the template initially had a V-type magnet configuration with two magnets arranged in the V-form within the pole. Since the tool focused on modeling flat configuration, the template was altered to simple flat. When modeling for electric loading in the tool (Python), the magnet had to be made thicker to prevent demagnetization by following the steps mentioned in Section 3.8. However, the MotorCAD environment does not provide the working points for the demagnetization curve, making it difficult to test the same. So, it was not known if the magnet was demagnetized.

To avoid the above discrepancies, this tool was used to replicate the machine sizing available in the journal [56] as a base case scenario presented in case study 2. An IPMSM with a flat-type magnet configuration was considered. The tool replicated the exact dimensions for the overall machine size and magnet dimensions, as seen in Tables 4.6 and 4.7 respectively. Despite these similarities, the dimensions of the slot were not available in the journal. Hence, these dimensions had to be validated by applying the same sizing parameters obtained from the tool to MotorCAD to test its credibility.

Table 4.8 shows the study on the flux densities at different critical parts of the machine. They show a large variation in the air gap flux density, leading to differences in other components. In FEM solvers like MotorCAD, the computation is done by meshing the

machine components into more minor elements called nodes, and the condition of the consecutive nodes is computed by the ones previous to it. The higher the number of nodal points, the higher the flux density accuracy [58]. This type of accuracy can be obtained in analytical models by having more reluctance elements [30], [40]–[42] but at the cost of computational resources. Since the core focus of this tool is the sizing parameters of the machine, it could get unnecessarily demanding for computation.

The torque and power depend on the magnetic and electric loading [12]. As observed in Table 4.9, the torque and power calculated by the MotorCAD are more accurate and closer to the journal value. This is because of the variation in air gap flux density. Additionally, the tool only estimates the magnetic torque as it models the flux using MEC. The reluctance torque occurs due to the saliency, which requires an advanced d-q axis computation. However, this does not account for the saturation points in the magnetic circuit [5].

5.3 Sensitivity Analysis

A sensitivity analysis was conducted to study the influence of sizing parameters on the machine's performance. The parameters chosen were air gap thickness [20], magnet width [6], pole-arc to pole-pitch ratio [19], [20], and magnet strength [6], as they directly influence the performance of the machine. One of the strategies to minimize cogging torque focuses on the right combination of slots and poles. This analysis was also conducted by varying fundamental frequencies. However, at higher frequencies, the number of poles increased, which was why the design of the magnet in the rotor was not geometrically feasible. Hence it is not presented in our findings.

As observed in Figures 4.1, 4.2, and 4.3, increasing air gap thickness decreased performance. As air is a non-magnetic material, the magnetic resistance is higher, which in turn requires higher energy for the flux to flow across the air gap. Thus, a lower force is generated. This reduces the electromagnetic torque and power generated by the machine. Since the magnetic flux flows in the path of least resistance, an increased leakage in the rotor core is seen in Figure 4.4.

The magnet width was varied by changing the K_m coefficient. Figures 4.5, 4.6 and 4.7 show that the increase in the magnet's width increased the flux density in the air gap and the machine's electromagnetic performance. A wider magnet generally increases the total magnetic flux, as the flux is a function of the area involved in flux transfer. More magnetic field lines extend across the air gap, enhancing the strength of the magnetic field.

Constraining the width of the magnet, the volume of the magnetic air barrier was varied by changing the pole-arc to the pole-pitch ratio (α), as given in Table 4.12. A decreased flux density was observed in Figure 4.8 when it was varied from 0.8 to 0.85. This is because the increased volume of the magnetic air barrier leads to higher leakage, which can be inferred from Figure 4.11. Since the flux density is decreasing, the torque and power of the machine is affected similarly.

Further, the air barrier volume was also decreased by varying α from 0.8 to 0.7. Therefore, there is an increase in the rotor core material. As seen in Figure 4.8, the flux density in the

air gap decreases [19] as the flux flows in the path of lower resistance, leading to higher leakage into the rotor core. This varying flux in the rotor core influences the saliency effect, allowing for the generation of reluctance torque [8]. This reluctance torque adds to the overall torque, increasing motor efficiency without needing extra input power.

Two magnet grades (N35 and N42) were considered, and their influence on the machine's performance was studied. The higher the magnet grade, the higher its remanence. Considering a constant volume of the magnet gave a higher flux density, as shown in Figure 4.12. For constant electric loading, higher magnetic loading led to better performance for the machine, as seen in Figure 4.13 and Figure 4.14.

5.4 Limitations

The accuracy of the tool is inherently restricted due to the analytical method applied. The study emphasized rapid and systematic approaches to size an EM, leading to necessary assumptions that simplified the design process.

Notably, thermal effects were not considered, and the design was strictly based on geometrical and mechanical constraints. Additionally, the tool lacks flexibility in modifying magnet configurations.

5.5 Future Scope

The evolving market for EMs necessitates advancements in design processes. To enhance accuracy, incorporating higher reluctance elements in the MEC or utilizing advanced statistical methods such as genetic algorithms, differential evolution, or conformal mapping can improve the estimation of the machine's electromagnetic performance.

Additionally, studying thermal effects is crucial for understanding magnet demagnetization characteristics and determining the cooling requirements necessary for optimal machine performance. Implementing a more dynamic BH curve analysis that considers an exponential method for various temperatures, along with updates on remanence flux density, can further refine the design.

While each magnet configuration in an EM is design-specific, adding functions that support the design criteria of different configurations can provide users with the flexibility to choose their desired setup.

6
Conclusion

This thesis presents a Python-based computational tool designed to optimize the sizing and parametrization of IPMSM, enabling rapid prototyping and minimizing iteration time. Two case studies validated the tool's capability to estimate essential machine dimensions and performance metrics, with sensitivity analyses providing insights into how variations in air gap thickness, magnet width, pole-arc to pole-pitch ratio, and magnet strength influence output characteristics.

The tool leverages analytical methods to establish correlations between design and performance parameters, acknowledging its limited accuracy compared to FEM solvers such as MotorCAD. While MotorCAD offers higher precision through its meshing technique, the Python tool provides a valuable and computationally efficient alternative for the preliminary design phase.

Despite some limitations, including the absence of thermal modeling and restricted adaptability for altering magnet configurations, the tool serves as a foundational platform for rapid IPMSM design iterations. It holds significant potential for advancing climate-neutral electric vehicle development.

Bibliography

[1] Z.-Q. Zhu and D. Howe, "Electrical machines and drives for electric, hybrid, and fuel cell vehicles," *Proceedings of the IEEE*, vol. 95, no. 4, pp. 746–765, 2007.

[2] M. Zeraoulia, M. E. H. Benbouzid, and D. Diallo, "Electric motor drive selection issues for hev propulsion systems: A comparative study," *IEEE Transactions on Vehicular technology*, vol. 55, no. 6, pp. 1756–1764, 2006.

[3] M. Aslan, A. B. Özpolat, İ. Cengiz, F. Eroğlu, and A. M. Vural, "Design and modelling of internal permanent magnet motor," *The International Journal of Energy and Engineering Sciences*, vol. 5, no. 2, pp. 80–104, 2020.

[4] Z. Zhu, D. Howe, E. Bolte, and B. Ackermann, "Instantaneous magnetic field distribution in brushless permanent magnet dc motors. i. open-circuit field," *IEEE transactions on magnetics*, vol. 29, no. 1, pp. 124–135, 1993.

[5] S. Morimoto, Y. Takeda, T. Hirasa, and K. Taniguchi, "Expansion of operating limits for permanent magnet motor by current vector control considering inverter capacity," *IEEE Transactions on Industry Applications*, vol. 26, no. 5, pp. 866–871, 1990. DOI: 10.1109/28.60058.

[6] L. Balasubramanian, N. A. Bhuiyan, A. Javied, A. A. Fahmy, F. Belblidia, and J. Sienz, "Design and optimization of interior permanent magnet (ipm) motor for electric vehicle applications," *CES Transactions on Electrical Machines and Systems*, vol. 7, no. 2, pp. 202–209, 2023.

[7] H. Zhuang, S. Zuo, Z. Ma, Q. Yu, Z. Wu, and C. Liu, "Analytical modeling of open-circuit air-gap flux density in interior permanent magnet machine," *IEEE Transactions on Magnetics*, 2023.

[8] M. Ibrahim and P. Pillay, "Aligning the reluctance and magnet torque in permanent magnet synchronous motors for improved performance," in *2018 IEEE Energy Conversion Congress and Exposition (ECCE)*, IEEE, 2018, pp. 2286–2291.

[9] T. Masuko and I. Miki, "A novel rotor structure of ipmsm with rare earth and ferrite magnets," in *2016 19th International Conference on Electrical Machines and Systems (ICEMS)*, IEEE, 2016, pp. 1–5.

[10] *Design of Stator - Induction Motors, BrainKart.com.* https://www.brainkart.com/article/Design-of-Stator---Induction-Motors_12308/.

[11] J. R. Hendershot and T. J. E. Miller, *Design of brushless permanent-magnet motors*. Oxford university press, 1995.

[12] J. Pyrhonen, T. Jokinen, and V. Hrabovcova, *Design of rotating electrical machines*. John Wiley & Sons, 2013.

[13] D. C. Hanselman, *Brushless permanent magnet motor design*. The Writers' Collective, 2003.

[14] R. Zhu, C. Di, X. Bao, and J. Liu, "Influence of the slots number combinations among the inner and outer stator on torque ripple in dual-stator permanent magnet synchronous motors," in *2021 24th International Conference on Electrical Machines*

and Systems (ICEMS), 2021, pp. 1137–1141. DOI: 10.23919/ICEMS52562.2021.9634503.

[15] T. Husain, C. Ma, N. Taran, and Z. Wan, "A comprehensive comparison of concentrated winding and distributed continuous winding machine topologies for hybrid electric vehicles," in *2021 IEEE Energy Conversion Congress and Exposition (ECCE)*, 2021, pp. 3683–3689. DOI: 10.1109/ECCE47101.2021.9595089.

[16] S. Ruoho *et al.*, "Modeling demagnetization of sintered ndfeb magnet material in time-discretized finite element analysis," 2011.

[17] G. Ofualagba, "The modeling and simulation of a microturbine generation system," *International Journal of Scientific & Engineering Research*, vol. 2, no. 7, pp. 1–7, 2012.

[18] S. Pan, "Rare earth permanent-magnet alloys' high temperature phase transformation," *Situ and Dynamic Observation and Its Application in Material Design*, 2013.

[19] Z. Zhu, S. Ruangsinchaiwanich, N. Schofield, and D. Howe, "Reduction of cogging torque in interior-magnet brushless machines," *IEEE Transactions on Magnetics*, vol. 39, Sep. 2003. DOI: 10.1109/INTMAG.2003.1230613.

[20] Z. Zhu and D. Howe, "Influence of design parameters on cogging torque in permanent magnet machines," *IEEE Transactions on energy conversion*, vol. 15, no. 4, pp. 407–412, 2000.

[21] L. Guo, C. Xia, H. Wang, Z. Wang, and T. Shi, "Improved equivalent magnetic network modeling for analyzing working points of pms in interior permanent magnet machine," *Journal of Magnetism and Magnetic Materials*, vol. 454, pp. 39–50, 2018.

[22] S. Paitandi and M. Sengupta, "Design, fabrication and parameter evaluation of a surface mounted permanent magnet synchronous motor," in *2014 IEEE International Conference on Power Electronics, Drives and Energy Systems (PEDES)*, IEEE, 2014, pp. 1–6.

[23] M. Farshadnia, *Advanced theory of fractional-slot concentrated-wound permanent magnet synchronous machines*. Springer, 2018.

[24] A. Proca, A. Keyhani, A. El-Antably, W. Lu, and M. Dai, "Analytical model for permanent magnet motors with surface mounted magnets," *IEEE Transactions on Energy Conversion*, vol. 18, no. 3, pp. 386–391, 2003. DOI: 10.1109/TEC.2003.815829.

[25] H.-J. Kim, J.-S. Jeong, M.-H. Yoon, J.-W. Moon, and J.-P. Hong, "Simple size determination of permanent-magnet synchronous machines," *IEEE Transactions on Industrial Electronics*, vol. 64, no. 10, pp. 7972–7983, 2017.

[26] M. Sundaram, M. Anand, J. Chelladurai, *et al.*, "Design and fem analysis of high-torque power density permanent magnet synchronous motor (pmsm) for two-wheeler e-vehicle applications," *International Transactions on Electrical Energy Systems*, vol. 2022, 2022.

[27] H.-W. Cho, K.-J. Ko, J.-Y. Choi, H.-J. Shin, and S.-M. Jang, "Rotor natural frequency in high-speed permanent-magnet synchronous motor for turbo-compressor application," *IEEE Transactions on Magnetics*, vol. 47, no. 10, pp. 4258–4261, 2011.

[28] G. Filomeno, B. Krüger, P. Tenberge, and D. Dennin, "Rapid electric motor sizing estimation for automotive application with statistical approach using catalog values," *Int. J. Mech. Eng. Robot. Res.*, vol. 9, no. 11, pp. 1457–1462, 2020.

[29] C. Mi, M. Filippa, W. Liu, and R. Ma, "Analytical method for predicting the air-gap flux of interior-type permanent-magnet machines," *IEEE Transactions on Magnetics*, vol. 40, no. 1, pp. 50–58, 2004.

[30] F. Mahmouditabar, A. Vahedi, and F. Marignetti, "The demagnetization phenomenon in pm machines; principles, modelling, and design considerations," *IEEE Access*, 2023.

[31] T. J. Miller, "Brushless permanent-magnet and reluctance motor drives," 1989.

[32] *BH Curves for Neodymium Magnets, KJ Magnetics Inc.* https://www.kjmagnetics.com/bhcurves.asp.

[33] Z. Wu, S. Zuo, S. Hu, and X. Hu, "Analytical modelling of air-gap magnetic field of interior permanent magnet synchronous motors," *IET Electric Power Applications*, vol. 14, no. 11, pp. 2101–2110, 2020. DOI: https://doi.org/10.1049/iet-epa.2019.0948. eprint: https://ietresearch.onlinelibrary.wiley.com/doi/pdf/10.1049/iet-epa.2019.0948. [Online]. Available: https://ietresearch.onlinelibrary.wiley.com/doi/abs/10.1049/iet-epa.2019.0948.

[34] F. Jimenez-Villacorta and L. H. Lewis, *Advanced permanent magnetic materials*, 2014.

[35] O. Gutfleisch, M. A. Willard, E. Brück, C. H. Chen, S. Sankar, and J. P. Liu, "Magnetic materials and devices for the 21st century: Stronger, lighter, and more energy efficient," *Advanced materials*, vol. 23, no. 7, pp. 821–842, 2011.

[36] S. Ruoho, E. Dlala, and A. Arkkio, "Comparison of demagnetization models for finite-element analysis of permanent-magnet synchronous machines," *IEEE Transactions on Magnetics*, vol. 43, no. 11, pp. 3964–3968, 2007.

[37] R. Szewczyk, "Technical b-h saturation magnetization curve models for spice, fem and mom simulations," *Journal of Automation, Mobile Robotics and Intelligent Systems*, vol. 10, no. 2, pp. 3–8, Feb. 2016. DOI: 10.14313/JAMRIS_2-2016/10. [Online]. Available: https://www.jamris.org/index.php/JAMRIS/article/view/378.

[38] B. Guo, Y. Huang, F. Peng, and J. Dong, "General analytical modeling for magnet demagnetization in surface mounted permanent magnet machines," *IEEE Transactions on Industrial Electronics*, vol. 66, no. 8, pp. 5830–5838, 2018.

[39] D. Torregrossa, A. Khoobroo, and B. Fahimi, "Prediction of acoustic noise and torque pulsation in pm synchronous machines with static eccentricity and partial demagnetization using field reconstruction method," *IEEE Transactions on Industrial Electronics*, vol. 59, no. 2, pp. 934–944, 2011.

[40] W. Bekir, O. Messal, and A. Benabou, "Permanent magnet non-linear demagnetization model for fem simulation environment," *IEEE Transactions on Magnetics*, vol. 58, no. 2, pp. 1–5, 2021.

[41] J. Farooq, S. Srairi, A. Djerdir, and A. Miraoui, "Use of permeance network method in the demagnetization phenomenon modeling in a permanent magnet motor," *IEEE transactions on magnetics*, vol. 42, no. 4, pp. 1295–1298, 2006.

[42] B. Sheikh-Ghalavand, S. Vaez-Zadeh, and A. H. Isfahani, "An improved magnetic equivalent circuit model for iron-core linear permanent-magnet synchronous motors," *IEEE Transactions on Magnetics*, vol. 46, no. 1, pp. 112–120, 2010. DOI: 10.1109/TMAG.2009.2030674.

[43] I.-S. Song, B.-W. Jo, and K.-C. Kim, "Analysis of an ipmsm hybrid magnetic equivalent circuit," *Energies*, vol. 14, no. 16, p. 5011, 2021.

[44] J.-Y. Song, J. H. Lee, D.-W. Kim, Y.-J. Kim, and S.-Y. Jung, "Analysis and modeling of permanent magnet variable flux memory motors using magnetic equivalent circuit method," *IEEE Transactions on Magnetics*, vol. 53, no. 11, pp. 1–5, 2017.

[45] R. Krishnan, *Permanent magnet synchronous and brushless DC motor drives*. CRC press, 2017.

[46] V. Ostović, *The Art and Science of Rotating Field Machines Design: A Practical Approach*. Jan. 2017, ISBN: 978-3-319-39079-6. DOI: 10.1007/978-3-319-39081-9.

[47] Š. Gans and J. Molnár, "Theoretical basis of a measurement method of magnetization curves,"

[48] M.-F. Hsieh and Y.-C. Hsu, "A generalized magnetic circuit modeling approach for design of surface permanent-magnet machines," *IEEE Transactions on Industrial Electronics*, vol. 59, no. 2, pp. 779–792, 2012. DOI: 10.1109/TIE.2011.2161251.

[49] M. Sharifian, K. Shaarbafi, J. Faiz, and M. Feyzi, "Slot fringing effect on the magnetic characteristics of the electrical machines," in *10th IEEE International Conference on Electronics, Circuits and Systems, 2003. ICECS 2003. Proceedings of the 2003*, vol. 2, 2003, 778–781 Vol.2. DOI: 10.1109/ICECS.2003.1301902.

[50] K. Yamazaki and M. Kumagai, "Torque analysis of interior permanent-magnet synchronous motors by considering cross-magnetization: Variation in torque components with permanent-magnet configurations," *IEEE Transactions on Industrial Electronics*, vol. 61, no. 7, pp. 3192–3201, 2014. DOI: 10.1109/TIE.2013.2278508.

[51] G.-H. Lee, S.-I. Kim, J.-P. Hong, and J.-H. Bahn, "Torque ripple reduction of interior permanent magnet synchronous motor using harmonic injected current," *IEEE Transactions on Magnetics*, vol. 44, no. 6, pp. 1582–1585, 2008. DOI: 10.1109/TMAG.2008.915776.

[52] C. Studer, A. Keyhani, T. Sebastian, and S. Murthy, "Study of cogging torque in permanent magnet machines," in *IAS'97. Conference Record of the 1997 IEEE Industry Applications Conference Thirty-Second IAS Annual Meeting*, IEEE, vol. 1, 1997, pp. 42–49.

[53] N. Bianchi, S. Bolognani, D. D. Corte, and F. Tonel, "Tubular linear permanent magnet motors: An overall comparison," *IEEE transactions on industry applications*, vol. 39, no. 2, pp. 466–475, 2003.

[54] C.-C. Hwang and Y. Cho, "Effects of leakage flux on magnetic fields of interior permanent magnet synchronous motors," *IEEE transactions on magnetics*, vol. 37, no. 4, pp. 3021–3024, 2001.

[55] C. Ma, J. Zhang, J. Wang, *et al.*, "Analytical model of open-circuit air-gap field distribution in interior permanent magnet machines based on magnetic equivalent circuit method and boundary conditions of macroscopic equations," *IEEE Transactions on magnetics*, vol. 57, no. 3, pp. 1–9, 2021.

[56] R. S Ambekar, "Design and development of high torque, compact and energy saver pmsm motor for hydraulic applications," *International journal of electrical and computer engineering systems*, vol. 13, no. 5, pp. 399–407, 2022.

[57] M. Sharifian, K. Shaarbafi, J. Faiz, and M. R. Feyzi, "Slot fringing effect on the magnetic characteristics of the electrical machines," vol. 2, Jan. 2004, 778–781 Vol.2, ISBN: 0-7803-8163-7. DOI: 10.1109/ICECS.2003.1301902.

[58] H. Gör and A. Dalcalı, "Design and optimization of a high-performance multi-barrier ipms motor for an electric scooter and bicycle," *Royal Society open science*, vol. 11, no. 3, p. 231 650, 2024.

A

Appendix

A.1 Datasheet for PM Modeling

The Neodymium magnet was used in this study. KJ Magnetics Manufacturer generated the datasheet required to model the BH curve [32].

Two magnet grades were used for sensitivity analysis N35 and N42 at temperature 20 °C. The BH curve data are as shown in Tables A.1 and A.2 respectively.

Table A.1: BH Curve data of N35 at 20 ° C [32]

B [kGauss]	12.10	2.82	1.96	1.30	0.75	0.17	0.00
H [kOersted]	0.00	-8.90	-9.71	-10.32	-10.80	-11.28	-11.42

Table A.2: BH Curve data of N42 at 20 ° C [32]

B [kGauss]	14.25	3.70	2.32	1.37	0.81	0.40	0.00
H [kOersted]	0.00	-10.00	-11.29	-12.18	-12.67	-13.00	-13.20

DEPARTMENT OF SOME SUBJECT OR TECHNOLOGY
CHALMERS UNIVERSITY OF TECHNOLOGY
Gothenburg, Sweden
www.chalmers.se

CHALMERS
UNIVERSITY OF TECHNOLOGY